Research Highlights

- 1D $Co_xNi_{(1-x)}Te$ MFs on nickel foam was synthesized using an oven based method.
- $Co_xNi_{(1-x)}Te$ MFs/NF works efficiently for both supercapacitor and OER application.
- The hybrid supercapacitor assembly $Co_xNi_{(1-x)}Te$ MFs//AC achieves highest areal capacity of 77.9 µAh cm^{-2} at a current density of 0.8 mA cm^{-2}.
- As an electrocatalyst, $Co_{0.75}Ni_{0.25}Te$ MF/NF only requires low over potential (η) of 289 mV to reach current density (j) of 10 mA cm^{-2} for OER.
- Density functional theory (DFT) calculations on the electronic and structural property of $Co_xNi_{(1-x)}Te$ MFs.

Design and fabrication of cobalt$_x$ nickel$_{(1-x)}$ telluride microfibers on nickel foam for battery type supercapacitor and OER study

Prangya Bhol,[a] Sayali Ashok Patil,[a] Narad Barman,[b] Erakulan ES,[b] Ranjit Thapa,[b] Manav Saxena,[a] Ali Altaee,[c] Akshaya K. Samal[a*]

[a]Centre for Nano and Material Sciences, Jain University, Jain Global Campus, Ramanagara, Bangalore 562112, India

[b]Department of Physics, SRM University –AP, Andhra Pradesh, India 522240

[c]Centre for Green Technology, School of Civil and Environmental Engineering, University of Technology Sydney, 15 Broadway, NSW 2007, Australia

*Email: s.akshaya@jainuniversity.ac.in

Graphical abstract

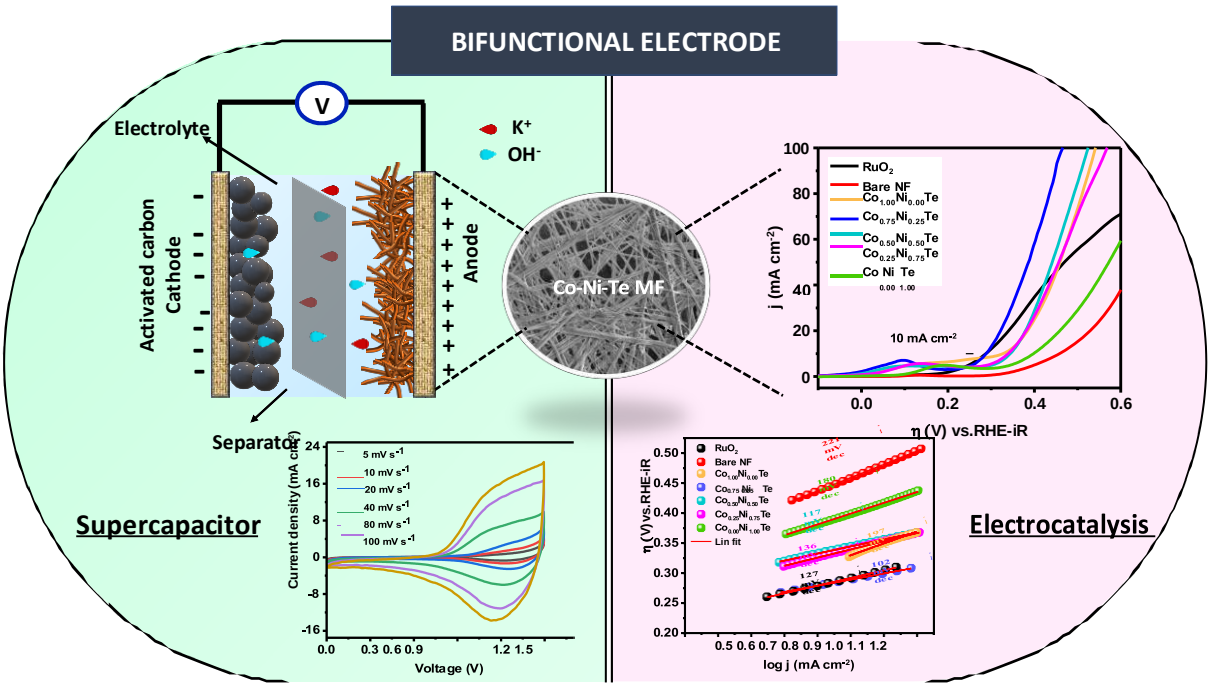

Design and fabrication of cobalt nickel$_{(1-x)}$ telluride microfibers on nickel foam for battery type supercapacitor and OER study

Prangya Bhol,[a] Sayali Ashok Patil,[a] Narad Barman,[b] Erakulan ES,[b] Ranjit Thapa,[b] Manav Saxena,[a] Ali Altaee,[c] Akshaya K. Samal[a*]

[a]Centre for Nano and Material Sciences, Jain University, Jain Global Campus, Ramanagara, Bangalore 562112, India

[b]Department of Physics, SRM University –AP, Andhra Pradesh, India 522240

[c]Centre for Green Technology, School of Civil and Environmental Engineering, University of Technology Sydney, 15 Broadway, NSW 2007, Australia

*Email: s.akshaya@jainuniversity.ac.in

ABSTRACT

Tellurium (Te) is a metal with the ability to function as a self-sacrificing template and exhibits strong chemical reactivity with counter metals. By the simple inward diffusion of metal ions on its surface it can form long one-dimensional (1D) architect. Utilizing this, a 1D Cobalt$_x$ Nickel$_{(1-x)}$ Telluride ($Co_xNi_{(1-x)}Te$) microfibers (MFs) on nickel foam (NF) substrate has been constructed for a bifunctional electrode application. The theoretical and experimental investigations on the $Co_xNi_{(1-x)}Te$ validates the $Co_{0.75}Ni_{0.25}Te$ superiority over other ratios. The synergistically caused effects at 3:1 Co/Ni ratio reactivity with Te enhance the microstructure bifunctional electrode property with excellent stability during long cycle operation. The density functional theory (DFT) calculations of $Co_{0.75}Ni_{0.25}Te$ revealed a better quantum capacitance due to the increased density of states near Fermi levels and achieved the enhanced OER activity because of increasing OH coverage. The assembled device $Co_{0.75}Ni_{0.25}Te$ MF//AC achieves outstanding energy storage performance with a maximum energy density of 50.8 Wh Kg^{-1} (58.4 µWh cm^{-2}) at a power density of 672.7 W Kg^{-1} (7773.5 µW cm^{-2}) and sustains the performance

up to 10,000 cycles, with a capacity retention of 90.1%. As an electrocatalyst, $Co_{0.75}Ni_{0.25}Te$ MF/NF requires a low overpotential (η) of 289 mV to reach a current density (j) of 10 mA cm^{-2} in 0.1 M KOH for OER.

KEYWORDS

Microfiber; Diffusion; Telluride; Supercapacitor; OER

1. Introduction

The urgent shipment of exhausting fossil fuels towards clean, renewable energy sources to fulfil the indispensable power supply requires a strong energy storage system and water splitting cells.[1, 2] This triggers the concerned researchers to study and build a potential energy storage and conversion device that could avoid the depletion of fossil fuels as well as maintain a uniform energy grid system. So far, supercapacitors have shown captivating features as compared to other energy storage devices in terms of power density, good stability, specific capacity, and fast charging and discharging properties.[3, 4] The commercially available symmetric supercapacitor has achieved a very low energy density of up to 4-6 Wh Kg^{-1}, which restricts its exploitation towards larger scale practical applications. Hybrid supercapacitors (HSCs) not only provide large capacity, but with a large voltage window, they can also deliver high energy and power densities. Water splitting through electrochemical techniques has been considered an effective approach because of its advantages, i.e., affordable cell setup, environmental friendliness, and zero carbon emission.[5] The oxygen evolution reaction (OER) is the crucial factor in overall electrocatalytic water splitting, but it's slow reaction kinetics and the overpotential (η) due to complex four-electron transfer frequently limit its use in practical applications.[6] Although commercially available, IrO_2 and RuO_2 have been active

electrocatalysts for OER, but their high price and low stability limit their use in widespread applications.[7, 8]

Diminishing the aforementioned drawbacks and building a competent electrode material that would work for both supercapacitors and OERs has become the most active research area currently. Factors such as morphology, conductivity, active electrode spots, oxygen defects, and material compositions all have a significant impact on electrode performance in energy storage and conversion applications. Hence, a suitable selection of elements, suitable synthesis technique, and optimized parameters would definitely help to achieve the goal. Metal oxides, hydroxides, and sulphides have been widely used in supercapacitors and water splitting applications.[9-11] These materials function via surface redox reactions between the electrolyte ions and the electrode material. Surface redox phenomena are strongly influenced by the core electronic structure as well as the conductivity of the electrode materials, which has a direct impact on electrochemical performance.[12, 13] Accordingly, optimization of the electrode material is critical. To upgrade the electrode performance, binary and ternary composites are synthesized by various approaches which can exhibit unique properties derived from the synergistic effect of their monometallic counterparts.[14] Lately, ternary Co-Ni oxide and sulphide composites have become a new hot spot for supercapacitor applications owing to their exclusive advantages like low cost, high specific capacitance, environmental friendliness, and unique redox properties.[15, 16] The analogous physical and chemical properties of Co and Ni and the miscibility of their ions in an aqueous electrolyte benefit their electrochemical properties. The binary Co-Ni oxides and sulphides have a lower optical band gap and better electrical conductivity compared to single-phase Ni/Co oxides and sulphides.[17, 18] Despite several advantages, their performance is greatly affected by their inadequate active spots, low conductivity, and stability.

Substituting the oxides and sulphides with conductive tellurides might develop a more stable structure, as the Te has a high anisotropic crystal growth tendency and serves as in situ templates for the one-dimensional (1D) growth of metal tellurides. Te is comprised of helical chains of atoms that are covalently bonded and subsequently united into a hexagonal lattice through van der Waals interactions, because of which it has a highly anisotropic crystal growth tendency towards one direction.[19] It has a tendency of self-sacrificing template and significant chemical reactivity with metals which can produce 1D metal telluride by simply inward diffusion of metal ions on Te template surface. Moreover, they are lesser electronegative than upper chalcogen element, which avoids the disintegration of layered structures and elongates in one direction, providing easier electron transport paths.[20] To date, transition metal tellurides, such as CoTe, Cu_7Te_4, NiTe, and FeTe: Fe_2TeO_5 have received a lot of attention recently as electrode materials owing to their well-organized anisotropic structure, high conductivity, electrochemical activity, and stability.[21-24] For example, Zhou and co-authors synthesized NiTe directly grown on nickel foam (NF) by adopting a hydrothermal route.[25] The electrode showed the highest specific capacitance of 804 F g^{-1} at a current density of 1 A g^{-1} in 3 M KOH electrolyte. However, the capacitance retention was only 81% up to 3000 cycles. Ye et al. reported a hydrothermal synthesis of CoTe nanosheets directly grown on carbon fiber paper.[26] In the asymmetric assembly of CoTe with activated carbon (AC), a highest specific capacitance of 67.3 F g^{-1} was achieved. The assembly reaches an energy density of 23.5 W h kg^{-1} at 1 A g^{-1}. By adding the redox additive $K_4Fe(CN)_6$ in the KOH electrolyte, the performance efficiency was promoted. A higher value of specific capacitance, 192.1 F g^{-1}, and an energy density of 67.0 W h kg^{-1} at 1 A g^{-1} were obtained with the addition of a redox additive. However, the analogous response was not reflected in the stability since the capacitance retention percent dropped from 92.3% to 80.7%.

Cinnamon-like La_2Te_3 thin film electrodes were grown by following the chemical bath deposition (CBD) method.[27] The electrode showed a high specific capacitance value of 469 F g^{-1} at a scan rate of 2 mV s^{-1}, and a capacitance drop of 27% was observed in 1000 cycles. In addition, Chen and co-workers obtained orthorhombic $CoTe_2$, which showed good OER catalytic performance. A low η of 241 mV was observed at a current density of 10 mA cm^{-2}, and a strong stability of more than 24 h was achieved.[28] In another report, Cu_7Te_4 nanowires were synthesized by a hydrothermal route, where the electrode catalyst displayed an η of 277 mV with a smaller Tafel slope of 33 mV dec^{-1} and exhibited good stability for 24 h.[29]

Nevertheless, these reports still suffer from low cyclic stability, low specific capacitance, and low energy density. Hence, a room is there to improvise the electrode behaviour based on choosing appropriate synthesis techniques, elements, and reaction conditions. A very few reports have explored the effects of concentrations of Co and Ni molar ratios on the morphology alteration of $Cobalt_x$ $Nickel_{(1-x)}$ Telluride ($Co_xNi_{(1-x)}Te$) grown directly on NF.[30] Moreover, the electronic and structural characteristics of $Co_xNi_{(1-x)}Te$ has not been illustrated briefly. The morphology obtained previously are mostly restricted to the nanometric range due to the complexity and time-consuming reaction steps. Prior research has not focused on the performance of bimetallic Co-Ni-Te materials as a bifunctional electrode for OER and supercapacitor application, but rather on either OER or supercapacitor application.[30-32] Hence, the optimization of the Co/Ni ratio reactivity with Te could explore some unforeseen properties and morphology that could deliver excellent electrochemical performance. To ascertain the impacts of the Co/Ni ratio reactivity with Te on the structural and electrical properties of $Co_xNi_{(1-x)}Te$ and investigate its bifunctional electrode property, more research is necessary.

It is a well-known fact that in the traditional slurry coating method, the presence of polymer binder often has a negative impact on the electrochemical efficiency. Therefore, it is better to breed the active material straight onto the current collector without any binder, which would save time, utilize the active material surface, have no loss of mass loading, high conductivity, and better rate performance. Herein, we report a simple and scalable one-step oven-based wet chemical method for synthesizing bimetal ternary composite 1D $Co_x Ni_{(1-x)}Te$ microfibers (MFs) directly grown on NF. The role of the Co/Ni molar concentration ratio reactivity with Te in the formation of various structures, as well as their electrochemical performance as bifunctional electrode, was thoroughly investigated. The Co/Ni ratios reactivity with Te significantly affect the surface structure and electrochemical behavior of metal telluride. The $Co_xNi_{(1-x)}Te$ MF grows with a dense 1D web-like network on NF, which facilitates strong diffusion of ions and electron transfer. [33, 34] As a result, the synthesized $Co_{0.75}Ni_{0.25}Te$/NF achieves an areal capacity of 188.9 µAh cm^{-2} (157.4 mAh g^{-1}) at the lowest current density of 0.8 mA cm^{-2} in a three-electrode system. In addition, an HSC with $Co_{0.75}Ni_{0.25}Te$/NF//AC as positive and negative electrodes was assembled, resulting in an excellent areal capacity of 77.9 µAh cm^{-2} (67.7 mAh g^{-1}). The assembled two-electrode system achieves a highest energy density of 50.8 Wh kg^{-1} (58.4 µWh cm^{-2}) at a power density of 672.7 W kg^{-1} (773.5 µW cm^{-2}). Moreover, excellent cyclic stability with capacity retention of 90.1% was obtained for 10,000 cycles. Furthermore, the electrode was tested for OER catalysis. $Co_{0.75}Ni_{0.25}Te$ only required an η of 289 mV to reach the current density (j) of 10 mA cm^{-2} with a Tafel slope of 102 mV dec^{-1}, confirming its suitability as a bifunctional electrode. Besides, the Co/Ni ratio-based electronic and structural properties of CoNiTe using the density functional theory (DFT) calculation demonstrated the superiority of $Co_{0.75}Ni_{0.25}Te$ based on quantum capacitance values and OH coverage range. The $Co_{0.75}Ni_{0.25}Te$ composition shows better quantum capacitance due

to the increased density of states near Fermi levels, and this composition also shows better OER activity with increasing OH coverage.

2. Experimental

2.1. Material and Method Used

All reactants were used as received without any additional purification. SRL, India, supplied the tellurium dioxide (TeO_2) powder, cobalt (II) nitrate hexahydrate ($Co(NO_3)_2.6H_2O$), and nickel (II) nitrate hexahydrate ($Ni(NO_3)_2.6H_2O$). Hydrazine hydrate ($N_2H_4.H_2O$) was purchased from Qualigen, India. Potassium hydroxide (KOH), ethanol (C_2H_5OH), hydrochloric acid (HCL), acetone, AC, and ruthenium (IV) oxide (RuO_2) were received from SD Fine, India. Nafion was brought from SIGMA Aldrich, India. Methods of characterization details have been given in section 1 of Supporting Information (SI).

2.2. Synthesis of 1D $Co_xNi_{1-x}Te$ MFs on NF

$Co_{0.75}Ni_{0.25}Te$ MFs were grown on NF by following an oven-based wet chemical method. Firstly, the NF was cleaned properly by ultrasonically agitating it in acetone, HCl (10%), water, and ethanol solutions to eradicate the oxidative layers and dust particles. In the typical reaction, $Co(NO_3)_2.6H_2O$ (15 mM), and $Ni(NO_3)_2.6H_2O$ (5 mM) were dissolved in 50 mL distilled water. TeO_2 (20 mM) was dissolved in 50 mL of ethanol. Each of the precursor solutions was prepared in separate beakers. To each of the stock solutions, 5 ml of $N_2H_4.6H_2O$ was added and sonicated well until a clear solution was obtained. Each of the stock solutions was mixed and sonicated well to prepare the growth solution for $Co_{0.75}Ni_{0.25}Te$ MFs. A piece of cleaned NF (1×2 cm^2) was hung and dipped inside the reaction mixture, of which 1×1 cm^2 was covered with heat resistant tape, and the rest of the area was kept exposed for the growth of active material. Subsequently, the solution was covered and kept in the oven for 16 h at 75 °C.

Afterwards, the reaction was allowed to cool at room temperature. The as-grown material on NF was collected from the beaker, washed with distilled water, and dried in the oven at 65 °C. The mass yield of active material grown on NF was 1.2 mg. The clean and dry electrode was pressed with 3-ton hydraulic pressure to obtain a uniform electrode surface. Optimization of Co/Ni ratios, i.e., (1:0), (3:1), (1:1), (1:3), and (0:1) were done to determine the structural and performance variance depending upon the precursor ratios and are represented as $Co_{1.00}Ni_{0.00}Te$, $Co_{0.75}Ni_{0.25}Te$, $Co_{0.5}Ni_{0.5}Te$, $Co_{0.25}Ni_{0.75}Te$, and $Co_{0.00}Ni_{1.00}Te$, and the concentration details are mentioned in Table 1.

Table 1: Concentrations of metal precursor for synthesizing $Co_xNi_{1-x}Te$ MFs on NF.

Material (Co:Ni)	**TeO_2 (mM)**	**$Co(NO_3)_2.6H_2O$ (mM)**	**$Ni(NO_3)_2.6H_2O$ (mM)**
$Co_{1.00}Ni_{0.00}Te$ (1:0)	20	20	0
$Co_{0.75}Ni_{0.25}Te$ (3:1)	20	15	5
$Co_{0.50}Ni_{0.50}Te$ (1:1)	20	10	10
$Co_{0.25}Ni_{0.75}Te$ (1:3)	20	5	15
$Co_{0.00}Ni_{1.00}Te$ (0:1)	20	0	20

2.3. Electrochemical Measurements

2.3.1. Three-electrode system

All the electrochemical measurements were done using the Electro Chem Origalys instrument, Austin, USA. Basic optimization of electrodes and working mechanisms were determined by cyclic voltammetry (CV), galvanic charge discharge (GCD), and electrochemical impedance spectroscopy (EIS) tests on a three-electrode system in 2M KOH electrolyte. During the experiment, Pt wire was used as the counter electrode, Ag/AgCl was used as the reference electrode, and active material grown on NF served as the working electrode.

2.3.2. Two-electrode system

After several studies, $Co_{0.75}Ni_{0.25}Te$ MF was finalized as the positive electrode for HSC assembly, with AC on NF as the negative electrode. To construct an HSC, a Swagelok cell was used for the device fabrication, which comprises two circular NF electrodes. The two corresponding electrodes were separated using a separator made of Whatman filter paper cut into a circular shape and dipped in 2 M KOH electrolyte. Before testing, the electrodes were soaked in the electrolyte. The areal capacity (C_a, mAh cm^{-2}) and specific capacity (C_s, mAh g^{-1}) of the electrodes were calculated from the GCD curves following eqn. (1).[35]

$$C_x = \frac{2I \int V dt}{3.6 \times x \times \Delta V} \quad (1)$$

Where, x denotes the mass (m, g) and area (a, cm^{-2}). I, Δt, and ΔV corresponds to current (A), discharge time (s), and potential window (V) after subtracting the internal resistance (IR) drop, respectively. To measure the energy density and power density, eqns (2) and (3) are used, respectively. In which E corresponds to the energy density (Wh Kg^{-1} or µWh cm^{-2}) and P corresponds to the power density (W kg^{-1} or µW cm^{-2}).[30]

$$E = \frac{I \int V dt}{3.6 \times x} \quad (2)$$

$$P = \frac{3600 \times E}{\Delta t} \quad (3)$$

2.3.3. OER Measurement

Standard measurements for OER were taken in the same three-electrode setup at a scan rate of 5 mV s^{-1} from 0 to 1 V vs. Ag/AgCl (active electrode area: 0.4 cm^2, mass loading: 0.9 mg). The η (overpotential against the RHE) was calculated by the following relationship:

$$\eta = E_{(Ag/AgCl)} + 0.197\ V + 0.059 \times pH - 1.236\ V - iR \qquad (4)$$

In which, $E_{(Ag/AgCl)}$ is the potential performed against reference electrode Ag/AgCl.

The electrochemical active surface area (ECSA) was measured by the following eqn (5):

$$ECSA = \frac{C_{dl}}{C_s} \qquad (5)$$

Based on the previously reported value for metal oxides and hydroxides in KOH, herein, C_s of value 0.04 mF cm^{-2} was taken for further calculation.[36] The C_{dl} (double layer capacitance) value is obtained from the slope plotted between capacitive current density and scan rates. Cyclic voltammograms were obtained from the double-layer region (0 to 0.1 V vs. Ag/AgCl) at different scan rates (5 to 100 mV s^{-1}). The roughness factor (RF) value was calculated by following eqn (6):

$$RF = \frac{ECSA}{a} \qquad (6)$$

2.4. Computational details

The DFT calculations were performed as implemented in the Vienna Ab-initio Simulation Package (VASP).[37] The exchange and correlation effect was included using Generalized Gradient Approximation (GGA) at Perdew-Burke-Ernzerhof (PBE) level.[38] The projected Augmented Wave (PAW) method was used to describe the potentials of the atoms.[39] A plane wave cut-off energy of 450 eV was used for the calculations. 5x5x1 k-points mesh using the

Monkhorst Pack scheme was considered for structural optimizations, and 9x9x1 k-points were used for density of states analysis. The calculations were performed until the total energy converged to less than 10^{-5} eV per atom and the maximum force converged to less than 0.05 eV/Å. The Grimme's DFT-D2 method was used for Van der Waal's dispersion correction.[40] Henkelman's bader charge analysis is used for estimating the charges on the atoms.[41] The CoTe unit cell was taken and Co atoms were replaced with Ni to attain the composition of $Co_{0.75}Ni_{0.25}Te$, and further, the bulk model was cleaved along the 101 plane. The lattice parameters of the super cell are a = 9.447 Å, b =15.636 Å, and it contains 18 Co-atoms, 6 Ni-atoms, and 24 Te-atoms. Additionally, the same structure with the ratio $Co_{0.50}Ni_{0.50}Te$ is also taken to compare the quantum capacitance activity. A vacuum of 15 Å was considered along the z-axis to remove any periodic interaction in the same direction.

3. Results and discussion

Well-grown $Co_xNi_{1-x}Te$ MFs were directly synthesized upon NF by using an oven-based wet chemical method without any assimilation of binder. The binder free approach benefited from growing the active material directly on the Ni substrate and engendering strong internal binding among active materials and the current collector.[42] Moreover, the porous NF with a huge surface area easily allows the material to penetrate as well as to grow inside part of the NF, reducing the chance of peeling off active material.[43] During the synthesis, each of the metal precursors was first reduced with $N_2H_4.H_2O$ and the corresponding solution were mixed along with the current collector (NF) and allowed to age at 75 °C for 16 h. Scheme 1 illustrates the schematic for growth of $Co_xNi_{1-x}Te$ MF on NF.

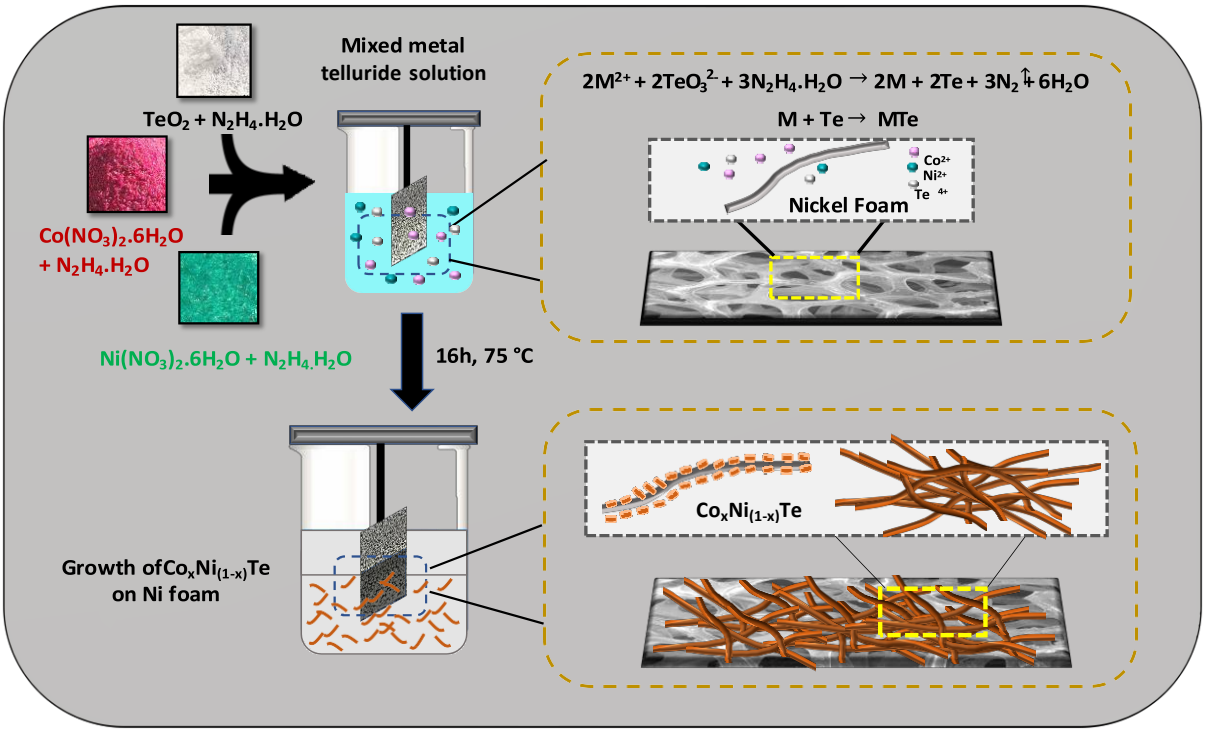

Scheme 1. Schematic illustration of synthesis of $Co_xNi_{1-x}Te$ on NF.

The reaction was kept for 16 h, and the anisotropic growth tendency of Te along one plane aids in the formation of the long fibril metal telluride structure. The self-scarification of Te templates and the alloying process were hypothesised as the reaction's mechanism. Firstly, metalloid oxyanion tellurite (TeO_3^{2-}) is formed when TeO_2 reacts with N_2H_4, followed by self-transformation into Te colloids such as amorphous Te (a-Te) and hexagonal Te (h-Te). The high free energy of a-Te allows it to diffuse into the basal plane of h-Te for growth in one direction.[34] Due to its high chemical reactivity with metals to generate metal telluride, h-Te then serves as a self-sacrificing template in the single pot reaction. During the alloying process, Co^{2+} /Ni^{2+} (M^{2+}) are simultaneously reduced to their corresponding zero oxidation states and then diffuse and react with the h-Te template to form metal tellurides. CoTe/NiTe were created, and during this phase, the development phase was constrained in a 1D environment. The reactions for the formation of CoTe and NiTe are shown below.

277 $2M^{2+} + 2TeO_3^{2-} + 3N_2H_4.H_2O \rightarrow 2M + 2Te + 3N_2\uparrow + 6H_2O$ (7)

278 $M + Te \rightarrow MTe$ (8)

279

280 To further support the function of Te in the development of 1D architect structures, Te was
281 investigated using field emission scanning electron microscopy (FESEM) analysis without any
282 counter metal ions in the reaction; the results of FESEM and energy dispersive spectrum (EDS)
283 are shown in Fig. S1. The inherent properties of anisotropic crystal structure growth of Te
284 towards a single plane led to the expected microfibril architect (Fig. S1A). The diameter of Te
285 MF was 110 $\pm$ 30 nm as shown in Fig. S1B. The presence of the Te element in EDS (Fig. S1C)
286 confirms the formation of pure Te MFs.

287

288 To investigate Te's reactivity with counter metal ions and its structure variance, the Co/Ni
289 ratios were optimized with Te in the reaction to finalize a better performing electrode. The
290 surface morphology of all the optimized metal tellurides was examined using FESEM analysis
291 and is shown in Fig. 1. The EDS (Fig. 1Aiii-Eiii) was performed by scratching out the as-grown
292 material from NF and drop casting it onto a Si wafer in order to evade the Ni elements from
293 the current collector and to identify the five samples. As observed from FESEM analysis (Fig.
294 1Ai and ii), the $Co_{1.00}Ni_{0.00}Te$ grew into long 1D microfibril structures. In EDS analysis (Fig.
295 1Aiii), the presence of Co and Te components was found, confirming the sample is purely
296 CoTe. Fig. 1Bi and ii show the FESEM images of $Co_{0.75}Ni_{0.25}Te$ MF/NF, which also display
297 long microfibril structure. The diameter of MF was measured, i.e., ~567 nm. From the FESEM
298 images, it was quite evident that, with the incorporation of higher Ni content (Fig. 1B-E) and
299 a simultaneous decrease in Co content to Te, the morphology changed from a dense microfibril
300 network to a broken and shorter MFs. The corresponding EDS analysis of $Co_{0.75}Ni_{0.25}Te$,
301 $Co_{0.50}Ni_{0.50}Te$, and $Co_{0.25}Ni_{0.75}Te$, as shown in Fig. 1Biii, Fig. 1Ciii, and Fig. 1Diii,

respectively, confirm the presence of Co, Ni, and Te. Te has a strong anisotropic 1D-growth tendency, and when combined with the proper counter metal ions during synthesis, it can create lengthy fibril-like metal telluride structures. This microfibril structure, when grown homogeneously on NF, is expected to enhance the electrochemical performance. Because Ni and Co have different growth tendencies and reaction rates with Te, as well as varying crystal structure stability, therefore there is a gradual change in morphology with changing Co/Ni ratios with Te.[44-46] The $Co_{0.00}Ni_{1.00}Te$ MF (Fig. 1Ei and ii) displays few granular particles and fragmented MFs, and Ni and Te elements were found in EDS (Fig. 1Eiii), supporting the synthesis of NiTe. Ni^{2+} at high concentrations has very rapid reaction kinetics with Te^{2-} because of which it results in broken MFs. Whereas, under the same reaction conditions, Co based materials are very stable and display their characteristic hexagonal crystal alignment with h-Te.[47-49] These results suggest that in the synthesis of $Co_xNi_{1-x}Te$ MF on NF, CoTe is the significant dominant cause for the formation of stable microfibril networks, and by adjusting the Co/Ni molar ratios with Te, the morphology may be tuned.

The inductively coupled plasma optical emission spectroscopy (ICP-OES) analysis was carried out for all the optimized Co/Ni molar ratios ($Co_xNi_{1-x}Te$ MFs) to determine the exact weight percentage of Co and Ni in the final obtained samples and are summarised in Table ST1 of SI. The molar ratio of the Co and Ni, elements follows the same pattern as the precursor $Co(NO_3)_2.6H_2O$ and $Ni(NO_3)_2.6H_2O$ ratio optimization because of the nearly identical weights of Co and Ni. The weight percentages of the Co and Ni elements in the $Co_{0.75}Ni_{0.25}Te$ were 37.41% and 12.57%, respectively, which is nearly same as the optimized 3:1 molar ratio.

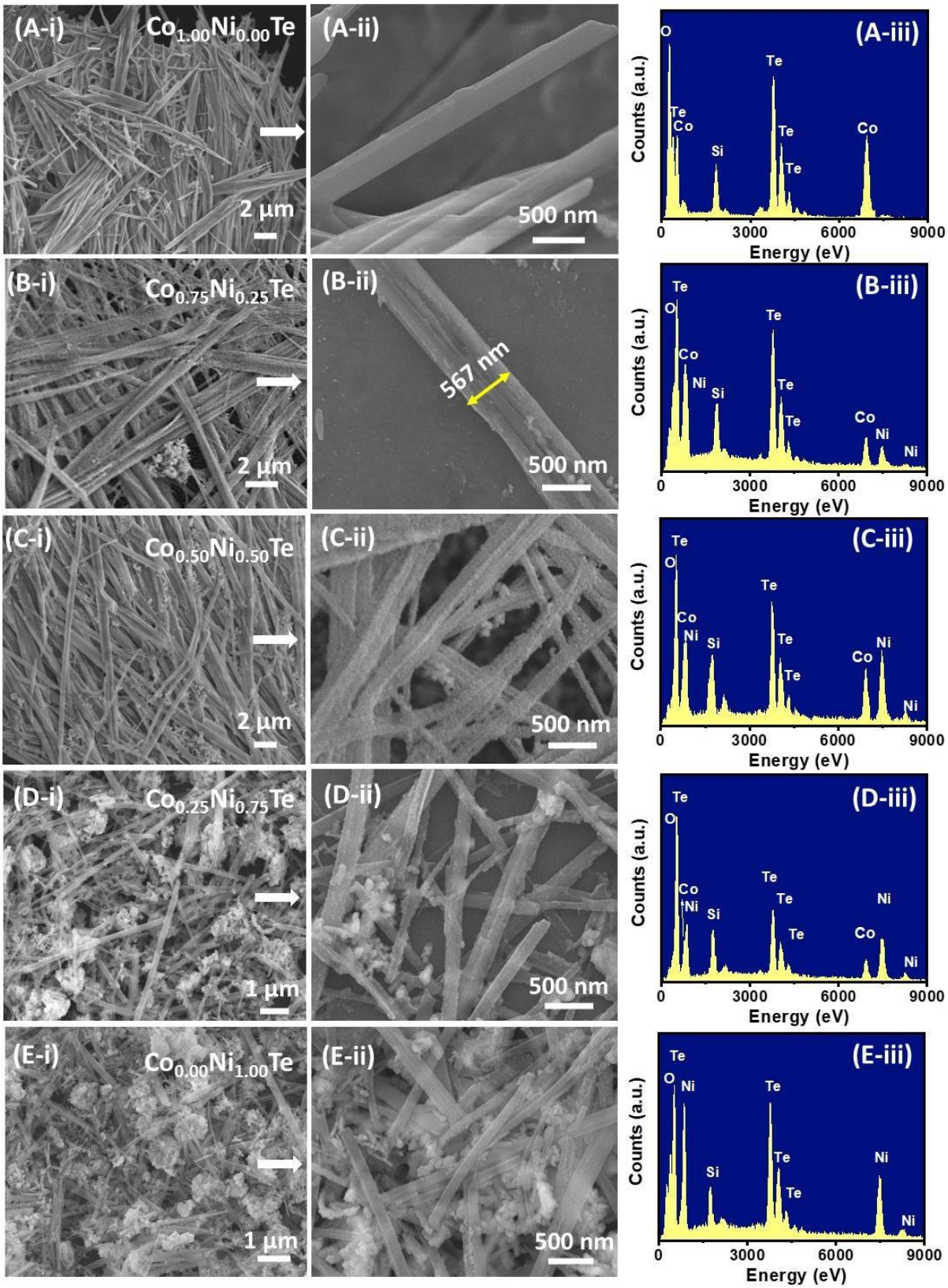

Fig. 1. FESEM image and EDS of (A-i-A-iii) $Co_{1.00}Ni_{0.00}Te$ MFs/NF, (B-i-B-iii) $Co_{0.75}Ni_{0.25}Te$ MFs/NF, (C-i-C-iii) $Co_{0.50}Ni_{0.50}Te$ MFs/NF, (D-i-D-iii) $Co_{0.25}Ni_{0.75}Te$ MFs/NF, and (E-i-E-iii) $Co_{0.00}Ni_{1.00}Te$ MFs/NF.

Fig. 2A shows the optical photograph of bare NF and deposited $Co_{0.75}Ni_{0.25}Te$ MFs on NF. On NF, active electrode material grew as a dark residue. Further, a detailed morphological study for $Co_{0.75}Ni_{0.25}Te$ MFs was done using the FESEM and TEM analyses. Fig. 2B confirms that the synthesized $Co_{0.75}Ni_{0.25}Te$ MFs are homogenously grown on NF. From the FESEM analysis shown in Fig. 2C, it was observed that the microfibril networks were densely spread over the current collector and the length of the MF was nearly 100 µm long. Fig. 2D displays a closer view of the microfibril dense network, and the diameter of the MF was measured from 30 different spots, and the corresponding histogram is represented in Fig. 2E. The MFs predominately displayed a diameter within the range of 550-1050 nm. Furthermore, the material was characterized by transmission electron microscopy (TEM). The growing material was scraped out of the NF and mixed with water to prepare the sample for TEM analysis. The solution was then dropped onto the shiny copper side of the carbon-coated copper grid and subjected to further analysis. A fibril structure with a diameter of 557 nm was evidenced from TEM analysis (Fig. 2F).

The lattice fringes measured from three different spots of the high-resolution TEM (HRTEM) image (Fig. 2G) are 0.21, 0.28, and 0.16 nm, which match with the planes of (102), (101), and (201), respectively, of CoTe and NiTe (ICDD no. 00-034-0420 for CoTe, ICDD no. 00-038-1393 for NiTe). Because NiTe and CoTe have comparable ionic radii, their hexagonal crystal configurations are almost identical, making it challenging to discern between CoTe and NiTe's interplanar spacing.

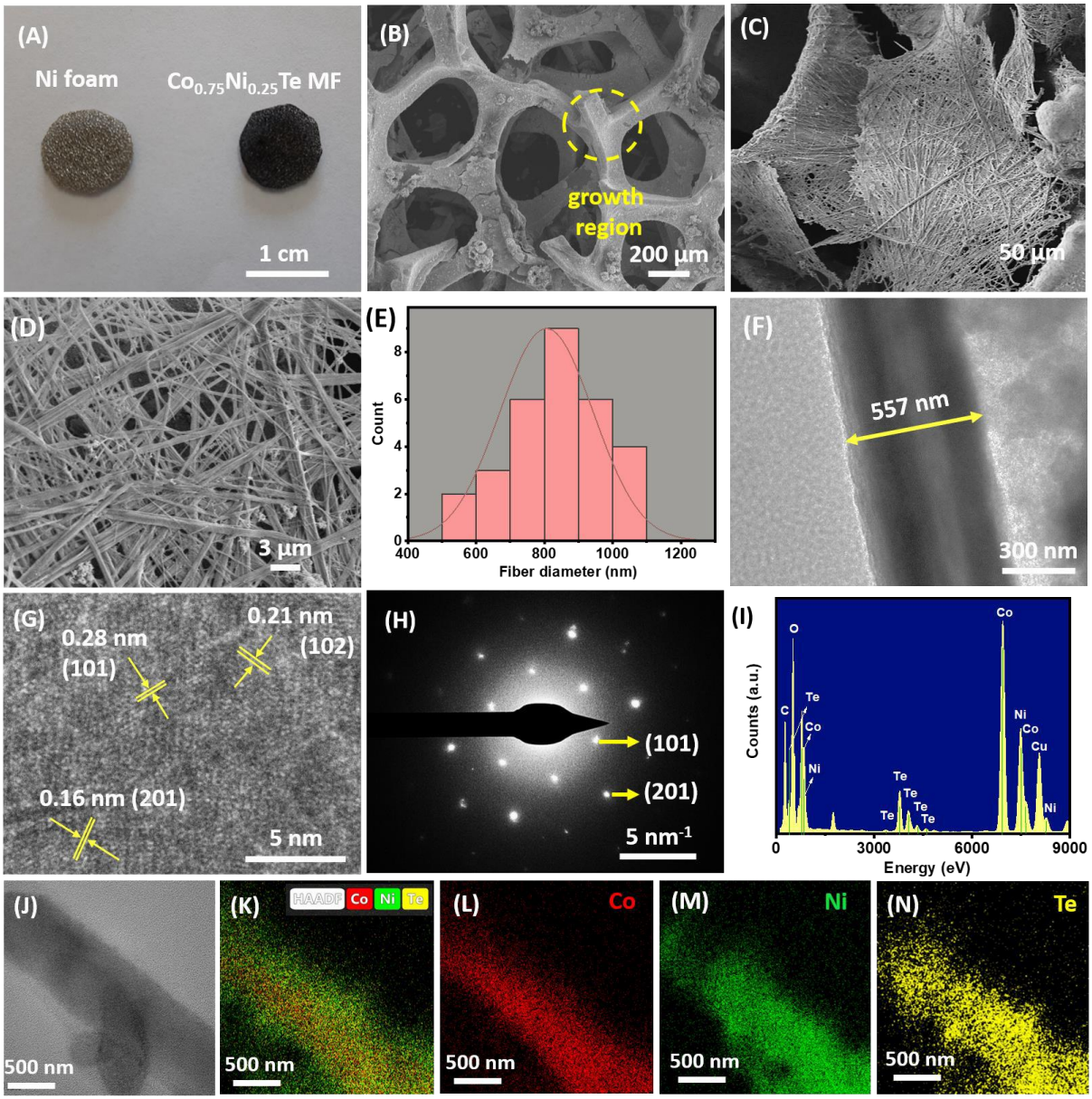

Fig. 2. (A) Optical photograph showing the growth of $Co_{0.75}Ni_{0.25}Te$ MFs on bare NF. (B-D) different magnifications of the FESEM images of $Co_{0.75}Ni_{0.25}Te$ MF grown on NF, (E) histogram showing the diameter of $Co_{0.75}Ni_{0.25}Te$ MF, (F) TEM image, (G) HRTEM image, and (H) SAED pattern of $Co_{0.75}Ni_{0.25}Te$ MF. (I) EDS showing presence of Co, Ni, and Te in $Co_{0.75}Ni_{0.25}Te$ MF, (J) TEM image of $Co_{0.75}Ni_{0.25}Te$ MF selected for elemental mapping, and (K-N) element mappings of Co, Ni, and Te, respectively, present in $Co_{0.75}Ni_{0.25}Te$ MF.

The selective area electron diffraction (SAED) pattern obtained from the HRTEM image is shown in Fig. 2H. The characteristic diffraction spots in the SAED pattern along with the obtained HRTEM image confirm its hexagonal crystalline nature. The corresponding diffraction spots from the patterns match the (101) and (201) planes of CoTe and NiTe (ICDD no. 00-034-0420-CoTe and ICDD no. 00-038-1393-NiTe). Fig. 2I shows the TEM EDS spectrum of $Co_{0.75}Ni_{0.25}Te$ MFs, the existence of Co, Ni, and Te, along with additional Cu, C, and O, peaks obtained from the sample grid, and unavoidable surface oxidation. To determine the Co, Ni and Te distribution along the MF, elemental mapping was carried out and it revealed an alloy type of homogeneous distribution of Co, Ni, and Te, throughout the sample (Fig. 2J-N).

To study the crystal phase of the synthesized $Co_xNi_{1-x}Te$ MF, and XRD pattern for all the optimized material was obtained by scratching out the active material from NF and is displayed in Fig. 3A. The XRD pattern for bare Te MF is shown in Fig. S1D. Te MF displays its obvious characteristic hexagonal crystal phase (ICDD no. 01-079-0736) with a lattice constant of a = b = 0.44 nm and c = 0.59 nm and a space group of P31 (152). The diffraction patterns for $Co_{1.00}Ni_{0.00}Te$ MF and $Co_{0.00}Ni_{1.00}Te$ MF demonstrate the formation of CoTe and NiTe in a hexagonal crystal phase matching the ICDD nos. 00-034-0420 and 00-038-1393, respectively. In the case of CoTe, a lattice constant of a = b = 0.38 nm and c = 0.53 nm with a space group of P63/mmc was determined, which was nearly the same as the obtained lattice constant values of NiTe, i.e., a = b = 0.39 nm, c = 0.53, with a space group of P63/mmc. While XRD patterns of $Co_{0.75}Ni_{0.25}Te$, $Co_{0.50}Ni_{0.50}Te$, and $Co_{0.25}Ni_{0.75}Te$ MF reveal the co-existence of CoTe and NiTe in a hexagonal crystal phase. Since Ni^{2+} and Co^{2+} have a similar ionic radius and crystal structure, the position of the CoTe and NiTe peaks obtained in the hexagonal phase are very close with same planes and are difficult to distinguish.[50, 51] All the peaks from the XRD

pattern were carefully examined, and it was observed that the peaks are broad and cover the 2θ range of both CoTe and NiTe. The characteristics peak at 2θ values of 26.4, 31.1, 33.3, 42.9, 46.5, 57.0, 58.2, 65.0, 76.4, and 77.2°, matching the (100), (101), (002), (102), (110), (201), (103), (202), (211), and (203) crystal planes of hexagonally structured CoTe and NiTe phases. A few additional peaks at 38.2, 40.4, and 52.0° correspond to (102), (110), and (103) crystal planes of unreacted h-Te matching the ICDD no. 01-079-0736. Te's typical lattice constants are a = b = 0.44 nm and c = 0.59 nm; these values are near those of h-CoTe and h-NiTe. Simply put, when Co and Ni interact with Te, a stable hexagonal crystal structure is produced, which Te prefers to grow, and as a result, long microfibrils are formed.

Furthermore, X-ray photoelectron spectroscopy (XPS) analysis is used to evaluate the chemical make-up and valence state of the synthesised MF. Fig. 3B's representation of the $Co_{0.75}Ni_{0.25}Te$ whole survey spectrum demonstrates the presence of Ni, Co, Te, C, O, and N. In the spectrum, the C peak originates from the pre-treatment, the O peak might arise because of the unescapable surface oxidation from the atmosphere, and the presence of N may be due to the residual hydrazine hydrate from the reaction. In the high-resolution spectra of both the Co 2p and the Ni 2p region, the spectra are deconvoluted into two spin-orbit doublets and two shake-up satellites referred to as the Sat. peak. The production of CoTe is confirmed by the peaks at binding energies of 781.5 eV and 796.8 eV in Fig. 3C that correspond to Co $2p_{3/2}$ and Co $2p_{1/2}$, respectively. [52] Furthermore, it exhibits the characteristic binding energy separation value of 15.3 eV for the Co^{2+} oxidation state.[53, 54] Two more peaks at 785.9 eV and 802.7 eV correspond to the Sat. peaks of CoO, which are obtained because of the surface oxidation on CoTe.[53] A similar observation was made in the case of Ni. Two substantial signals in the Ni 2p area (Fig. 3D), corresponding to the Ni $2p_{3/2}$ and Ni $2p_{1/2}$ of the Ni-Te bond, respectively, at 855.8 eV and 873.1 eV, indicate the Ni^{2+} oxidation state. The peaks at 861.9 eV and 880.5 eV

correspond to the Sat. peaks, implying the existence of a Ni-O bond because of the surface oxidation of NiTe. Moreover, it shows a characteristic binding energy separation value of 17.3 eV.[55] In the Te 3d spectrum of Fig. 3E, the peak fitting analysis depicts Te to be in a -2 and +4 oxidation state. The peaks at 572.4 eV and 582.8 eV correspond to the Te $3d_{5/2}$ and Te $3d_{3/2}$ of Te^{2-}, with a binding energy separation value of 10.4 eV. Besides, the peaks located at 575.7 eV and 586.1 eV indicate the development of TeO_2 because of the surface oxidation of Te species.[56] The presence of Co^{2+}, Ni^{2+}, and Te^{2-} strongly validates the existence of both CoTe and NiTe in the sample.

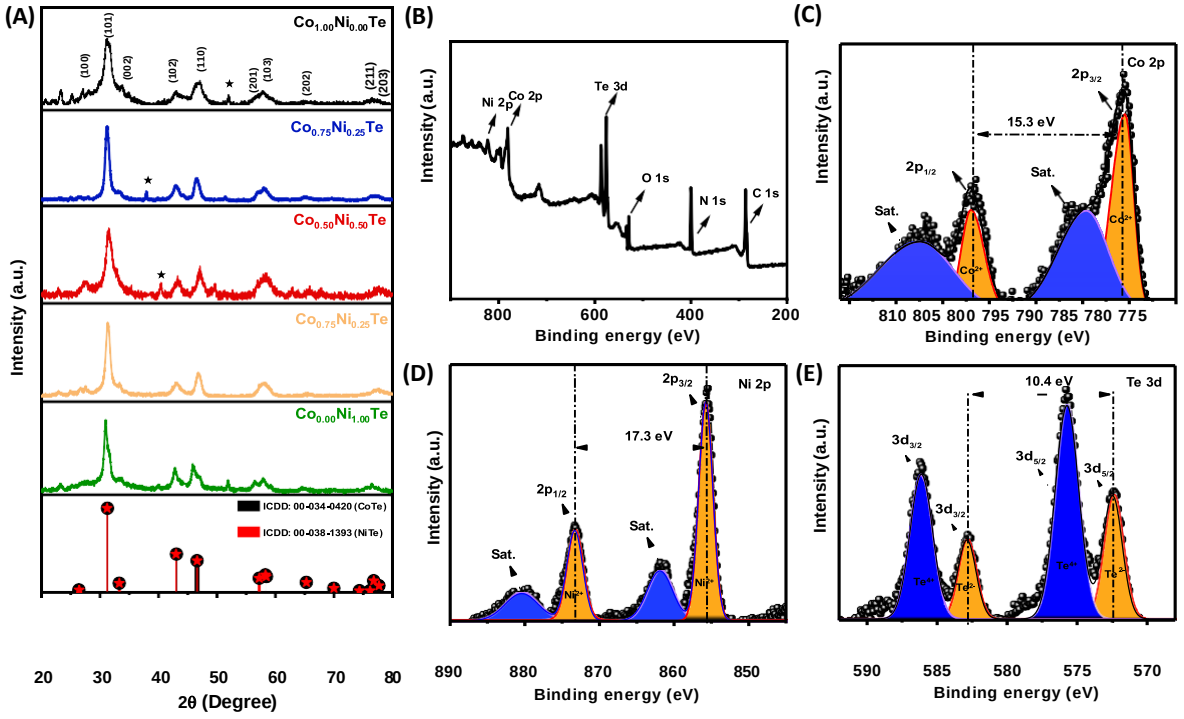

Fig. 3. (A) XRD patterns for all optimized $Co_xNi_{(1-x)}Te$ MF materials, (B) XPS full survey spectrum, (C) Co 2p region, (D) Ni 2p region, and (E) Te 3d region of $Co_{0.75}Ni_{0.25}Te$ MFs.

The zeta potential of $Co_{0.75}Ni_{0.25}Te$ MF in water medium was carried out. The distribution curve shown in Fig. S2A indicates the positive zeta potential of synthesised $Co_{0.75}Ni_{0.25}Te$ MFs with a value of 14.0 mV. The positive zeta potential of $Co_{0.75}Ni_{0.25}Te$ MFs demonstrates the good physical stability of the colloidally suspended particles because of the electrostatic

425 repulsion among each other. By using dynamic light scattering (DLS) measurement, the

hydrodynamic diameter of the synthesised $Co_{0.75}Ni_{0.25}Te$ MF was discovered to be 1644.7 nm, as shown in Fig. S2B. The hydrodynamic diameter usually tends to be greater than the actual particle diameter that was observed in FESEM analysis as it is the sum of the $Co_{0.75}Ni_{0.25}Te$ MF core diameter and the diffused electric double layer of water molecules, as illustrated in Fig. S2C.

3.1. $Co_xNi_{1-x}Te$ MF/NF electrochemical performance

3.1.1. Three-electrode testing

To explore the electrochemical performance of all synthesized samples, CV, GCD, and EIS tests were performed in the three-electrode setup in 2 M KOH aqueous electrolyte. Fig. 4A shows the comparative CV plots of all the optimized $Co_xNi_{1-x}Te$/NF ratios and bare NF recorded at a scan rate of 100 mV s^{-1} with a working window of 0 to 0.5 V. The capacitive potential of the electrode could be determined from the area under the of the CV plot. As shown in the CV plot, the bare NF contributed a very small integral area when compared to the synthesized $Co_xNi_{1-x}Te$MF/NF, confirming that the synthesized $Co_xNi_{1-x}Te$MF/NF contributes the majority of capacity. All the optimized electrodes showed prominent redox peaks (vs. Ag/AgCl) in their CV plots, indicating a Faradaic charge storage mechanism dominated by some noteworthy changes in the current intensity and peak positions, which are because of the variance in mass loading as well as the Co/Ni ratio. The observed reversible redox peaks originate because of the Faradaic redox transition between Co^{2+}, Co^{3+}, and Co^{4+} of CoTe and Ni^{2+} and Ni^{3+} of NiTe in the presence of OH^- ions in an alkaline electrolyte, respectively, and the reactions are as follows:[30, 57]

$$CoTe + OH^- \rightleftharpoons CoTeOH + e^- \quad (9)$$

$$CoTe(OH) + OH^- \rightleftharpoons CoTeO + H_2O + e^- \quad (10)$$

$$NiTe + OH^- \rightleftharpoons NiTeOH \quad (11)$$

The structural features and conductivity of the material depend upon the Telluride MF. Moreover, the lower electronegativity of Te as compared to the upper chalcogen group element gives an advantage, i.e., a frailer chemical bond with its bonding electrons, resulting an unstable electronic state of the compound, making it more active towards redox reactions. Even though the electrodes constitute both Co and Ni, they could not separate their corresponding redox peaks because of the high current density arising from a reversible Faradaic redox reaction, leading to the overlap of peaks. The current intensity obtained from the $Co_{0.75}Ni_{0.25}Te$/NF CV profile was higher with a larger curve area compared to all other optimized Co/Ni ratios, suggesting that $Co_{0.75}Ni_{0.25}Te$/NF is the best performing electrode. In fact, it was observed that with a simultaneous increase in Ni content and a decrease in Co content in the metal telluride, the curve area first increases and then gradually decreases. The charging and discharging behaviour of all the optimized electrodes was further verified from GCD analysis, at a constant current density of 3 mA cm^{-2} over a potential window from 0 to 0.5 V, as shown in Fig. 4B. The GCD profiles for all the optimized electrodes show a charging discharging plateau (nonlinear curve) that reciprocates the Faradaic charge storage mechanism, consistent with the CV analysis. The curve behaviour obtained from Co_xNi_{1-x}TeMF/NF is quite similar to that of Ni and Co-based battery-type electrodes.[18, 58] The discharging time in the charging and discharging curve came out to be different for different optimized ratios. As observed in the CV analysis, the GCD curves followed the same trend. The discharging time increases until the (3:1) ratio of Co/Ni ($Co_{0.75}Ni_{0.25}Te$/NF) and then gradually decays with the increase of Ni content, ensuring that $Co_{0.75}Ni_{0.25}Te$/NF is a better electrochemical performer. The areal capacity of all the optimized electrodes is measured following eqn (1) at a fixed current density of 3 mA cm^{-2}, and the corresponding plot is shown in Fig. 4C. $Co_{1.00}Ni_{0.00}Te$/NF, $Co_{0.75}Ni_{0.25}Te$/NF, $Co_{0.50}Ni_{0.50}Te$/NF, $Co_{0.25}Ni_{0.75}Te$/NF, and $Co_{0.00}Ni_{1.00}Te$/NF with mass

loadings of 1.1, 1.2, 1.4, 1.5, and 1.3 mg cm^{-2}, respectively, yielded an areal capacity of 39.5, 90.1, 83.1, 61.8, and 37.0 µAh cm^{-2}. The $Co_{0.75}Ni_{0.25}Te$/NF showed the highest areal capacity among all the electrodes. The mass loading of the electrode material is a central factor in influencing the electrochemical performance, so specific capacity was also computed using eqn (1) at a constant current density of 3 mA cm^{-2} for $Co_{1.00}Ni_{0.00}Te$/NF, $Co_{0.75}Ni_{0.25}Te$/NF, $Co_{0.50}Ni_{0.50}Te$/NF, $Co_{0.25}Ni_{0.75}Te$/NF, and $Co_{0.00}Ni_{1.00}Te$/NF to ensure the best performing electrode. Fig. S3 shows that $Co_{0.75}Ni_{0.25}Te$/NF achieved the highest specific capacity value of 75.0 mAh g^{-1} as compared to all other optimized electrodes. And based on these values, the 3:1 ratio of Co/Ni for $Co_xNi_{1-x}Te$/NF stands out among all the optimized ratios, confirming it to be the best performing electrode.

The desirable electrochemical performance is achieved because of the superior electrical conductivity of the Te-based composition, the synergistic effect associated with Co, Ni, and Te elements, and the structural design of microfibrils. The anisotropic growth tendency of Te avoids the disintegration of layered structures and favours the growth along one direction, resulting in large microfibril networks on NF. Such growth generates a 1D electron transport path, a large surface area, a strong ion interpenetrating network, a shorter diffusion space, and sufficient exposure of active electrode sites towards the electrolyte. When the nickel content was zero, $Co_{1.00}Ni_{0.00}Te$/NF induced the formation of a microfibril network on NF, which aids the diffusion of electrolyte ions inside the deep core of the electrode to participate in the redox reactions. Further, when the Ni content was increased ($Co_{0.75}Ni_{0.25}Te$/NF), it positively influenced the electrochemical performance inherited from the high theoretical capacitance of Ni-based compounds along with the microfibril structure.[59, 60] However, the same trend couldn't be followed when Ni content was further increased ($Co_{0.50}Ni_{0.50}Te$/NF to $Co_{0.00}Ni_{1.00}Te$/NF). This happened because at higher Ni contents, nanoparticles along with

microfibril structures grew and the fibril network started breaking, which negatively influenced the electrochemical performance. Moreover, the synergistic effect at a 3:1 ratio of Co and Ni with Te was more effective as compared to other optimized ratios. Therefore, the appropriate Co/Ni ratio along with conductive Te in a wide microfibril network provides good electroactive spots, a dense interpenetrating network, and minimal diffusion space that would be beneficial for energy storage efficiency.[61, 62] Since the $Co_xNi_{1-x}Te$ MF is directly grown on the conductive NF, it provides adequate contact for the electrode on the inner side of the current collector, plus it evades the use of any polymer binder that could have arisen dead volumes on the electrode surface, enhancing the electrochemical performance.[63]

To confirm the veracity of the superior electrical conductivity of Te-based composition, EIS measurements were carried out for all five optimized $Co_xNi_{1-x}Te$ MF/NF samples over the frequency range of 0.1 Hz to 100 KHz at an open circuit potential of 5 mV. The Nyquist curves are shown in Fig. 4D, and a magnified view is in the inset of the plot. As can be observed, the small semi-circular zone, which is present in all EIS plots at a higher frequency range corresponds to the Faradaic charge transfer resistance (R_{ct}). R_{ct} arises from the electrode-electrolyte interface, and is measured by the diameter of the semi-circular region. The linear part in the low-frequency region of the plot indicates the capacitive characteristic, and the horizontal intercept on the real axis (X-axis) of the plot represents the solution resistance (R_s).[64, 65]

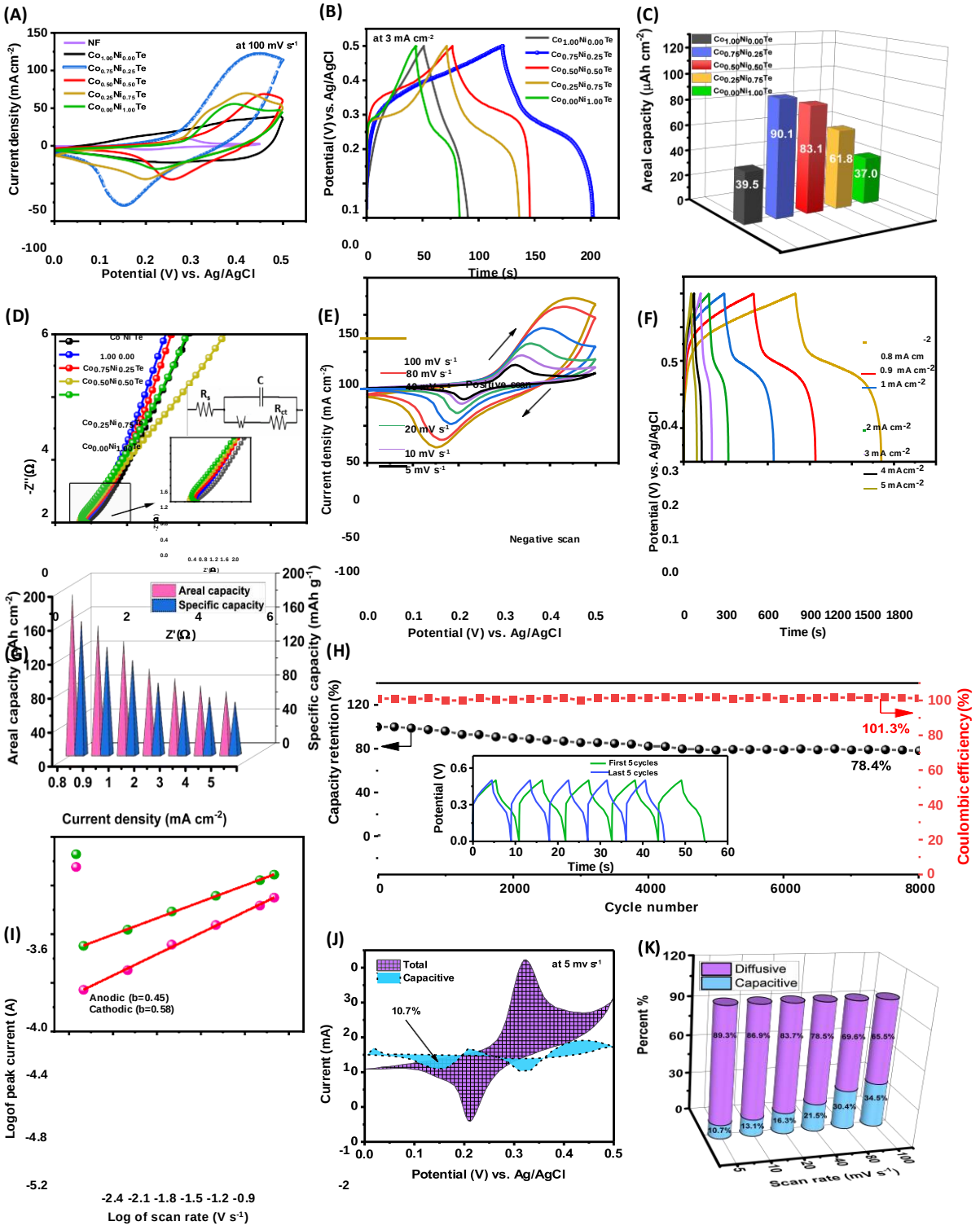

521

522 **Fig. 4.** Electrochemical testing for all the optimized Co_xNi_{1-x}TeMF/NF electrodes in a three-
523 electrode system: (A) CV curves, (B) GCD curves, (C) Areal capacity at a current density of 3
524 mA cm^{-2}, and (D) the EIS curve. Electrochemical testing for $Co_{0.75}Ni_{0.25}$Te/NF (E) CV curves
525 of at different scan rates, (F) GCD curves of at different current densities. (G) Areal capacity

and specific capacity at different current densities. (H) Cyclic stability and coulombic efficiency of $Co_{0.75}Ni_{0.25}Te$/NF at a current density of 10 mA cm^{-2}, (I) plot of log (peak current) vs. log (scan rate), (J) CV plot showing diffusive and capacitive controlled contributions at a

scan rate of 5 mV s^{-1}, and (K) bar graph plot of diffusive and capacitive contributions under different scan rates of 5-100 mVs^{-1}.

Of particular note, the magnitudes of R_s and R_{ct} obtained for all $Co_xNi_{1-x}Te$ MF/NF samples were found to be similar with some minor differences. The corresponding fitted circuit of the EIS curve is shown in the inset of Fig. 4D. Previous reports for Ni-Co oxides have validated the higher conductivity of bimetallic Co-Ni at a 3:1 ratio as compared to other ratios.[17, 18] A similar observation was obtained in the case of $Co_xNi_{(1-x)}Te$ MF. The R_s values for the $Co_{1.00}Ni_{0.00}Te$/NF, $Co_{0.75}Ni_{0.25}Te$/NF, $Co_{0.50}Ni_{0.50}Te$/NF, $Co_{0.25}Ni_{0.75}Te$/NF, and $Co_{0.00}Ni_{1.00}Te$/NF electrodes are 0.82, 0.71, 0.80, 0.84, and 0.84 Ω, respectively. The Nyquist plot of $Co_{0.75}Ni_{0.25}Te$/NF showed the smallest semi-circular region, and the straight line had a greater inclination toward the imaginary axis in the low frequency range. The R_{ct} values for $Co_{1.00}Ni_{0.00}Te$/NF, $Co_{0.75}Ni_{0.25}Te$/NF, $Co_{0.50}Ni_{0.50}Te$/NF, $Co_{0.25}Ni_{0.75}Te$/NF, and $Co_{0.00}Ni_{1.00}Te$/NF electrodes are 0.41, 0.36, 0.43, 0.44, and 0.45 Ω, respectively. In brief, the lowest value of R_{ct} and R_s for $Co_{0.75}Ni_{0.25}Te$/NF signifies the effective contact of the $Co_{0.75}Ni_{0.25}Te$ surface with the current collector NF and signify its better conductivity among all other optimized electrodes.

Based on the preliminary studies, it was realized that the overall performance of the $Co_xNi_{1-x}Te$MF/NF electrode is not based on any single cause but the interplay of multiple causes like composition ratio, morphology, and conductivity. As observed, $Co_{0.75}Ni_{0.25}Te$/NF stood out in all the preliminary testing and was recognized as the final optimized electrode for further electrochemical testing. Fig. 4E presents the scan rate dependent CV plots of $Co_{0.75}Ni_{0.25}Te$/NF ranging from 5-100 mV s^{-1}. With the increase in scan rate, the current intensity and the integral area of the CV plot were increased. Because of the polarization of the electrode, the peak

positions of oxidation and reduction gradually move toward higher positive and negative potentials, respectively. However, at a high scan rate of 100 mV s^{-1}, the shape of the plot remains unaltered without any disappearance of redox peaks, with a peak to peak (ΔE_p) value of 0.29 V, indicating the quasi-reversible characteristic of $Co_{0.75}Ni_{0.25}Te$/NF. Fig. 4F shows a distorted triangular charging and discharging behaviour for $Co_{0.75}Ni_{0.25}Te$/NF applied at different current densities due to reversible redox interactions.[66]

The areal capacity and specific capacity, respectively, were calculated from the discharging curve at different current densities, as shown in Fig. 4G. The areal capacity calculated for the $Co_{0.75}Ni_{0.25}Te$ MF/NF electrode corresponding to current densities of 0.8, 0.9, 1, 2, 3, 4, and 5 mA cm^{-2} is 188.9, 152.4, 133.8, 101.6, 90.0, 81.6, and 75.0 µAh cm^{-2}, respectively. The observed specific capacity values of the $Co_{0.75}Ni_{0.25}Te$/NF electrode are 157.4, 127.0, 111.5, 84.6, 75.0, 68.0, and 62.5 mAh g^{-1}. With the increase in current density from 0.8 to 5 mA cm^{-2}, the electrode preserved 39.7% of its initial capacity, confirming the excellent rate performance of $Co_{0.75}Ni_{0.25}Te$ MF/NF. The highest achieved mass ratio capacity value for all the optimized electrode materials while comparing them with the reported Ni and Co based tellurides is given in Table ST2. To evaluate the long-cyclic stability of $Co_{0.75}Ni_{0.25}Te$/NF, repeated GCD analysis at a constant current density of 10 mA cm^{-2} was carried out for 8,000 cycles in the three-electrode setup. Fig. 4H shows the coulombic efficiency and capacity retention percentage with increasing cycle number, and the inset of the figure shows the GCD curve of the first five and last five cycles. The $Co_{0.75}Ni_{0.25}Te$ MF/NF electrode maintains excellent capacity retention of 78.4% and coulombic efficiency of 101.3% even after 8,000 cycles. For a detailed illustration of the capacity decay of $Co_{0.75}Ni_{0.25}Te$, the CV curve at a scan rate of 40 mV s^{-1} and the EIS plot of the $Co_{0.75}Ni_{0.25}Te$ before and after the stability test are shown in Fig. S4A and B, respectively. The $Co_{0.75}Ni_{0.25}Te$ MF/NF exhibits a decrease in the

discharge time as well as in the integral area of the CV curve following the stability test because directly dipping the electrode into KOH electrolyte makes it more wettable and raises the risk of active electrode material peeling off during the continuous charge discharge test, which lowers the stability. The R_s and R_{ct} values acquired from the EIS test of $Co_{0.75}Ni_{0.25}Te$ are 1.01 and 0.42 Ω, respectively; these values are slightly higher than the R_s and R_{ct} values obtained from the before stability test, which were 0.71 and 0.36 Ω, respectively.

A theoretical investigation based on the CV curves was carried out by applying the power law. [67, 68] The peak current of an electrode has an exponential relationship with respect to the scan rate. The equation is represented below:

$$i = av^b \quad (12)$$

$$\log(i) = \log(a) + b\log(v) \quad (13)$$

In which, i and v denote the current (A) and scan rate (Vs^{-1}), respectively, a and b are two constants. In power law, the exponent "b" is the crucial factor in determining the charge storage mechanism for an electrode. The slop obtained from the fitted line of the plot between log (peak current) vs. log (scan rate) gives the b value. An ideal supercapacitor displays b value of "1", which corresponds to surface capacitive kinetics, while an ideal battery displays b value of "0.5" because of diffusion intercalation kinetics. Fig. 4I shows the plot between log (peak current) vs. log (scan rate), and the slops (b values) obtained from the $Co_{0.75}Ni_{0.25}Te$/NF with respect to the anodic and cathodic plots are 0.45 and 0.58, respectively, indicating a diffusive controlled process is dominating in the $Co_{0.75}Ni_{0.25}Te$/NF. The plot of peak current positions with respect to the square root of scan rate shown in Fig. S5 preserves a linear relationship, indicating a diffusion-controlled reaction to be dominant at the electrode-electrolyte interface. At a specific voltage, the total current i(V) is contributed by two terms of scan rate, constituting capacitive-controlled and diffusive-controlled processes, and can be expressed as:

$$i(V) = k_1\upsilon + k_2\upsilon^{0.5} \quad (14)$$

The first half of the equation $k_1\upsilon$ is the contribution of current from the surface related capacitive-controlled reaction, and the second half of the equation $k_2\upsilon^{0.5}$ is the Faradaic current contribution.[69] By dividing $\upsilon^{0.5}$ on both the sides of the equation, a straight-line equation "y = mx + c" is obtained.

$$\frac{i(V)}{\upsilon^{0.5}} = k_1\upsilon^{0.5} + k_2 \quad (15)$$

The values of constants k_1 and k_2 are measured by fitting a line to the plot of $\frac{i(V)}{\upsilon^{0.5}}$ vs $\upsilon^{0.5}$, where k_1 and k_2 are obtained from the slope and intercept of the line, respectively.[70] Fig. 4J shows the graphical representation of the capacitive contributions in the CV plot at a scan rate of 5 mV s^{-1}, respectively. The sky region and violet regions in the CV plot indicate the capacitive and experimental current contributions, respectively. From both the curves, it was realized that the diffusive process is the major current contributing factor from the $Co_{0.75}Ni_{0.25}Te$/NF electrode.

A comparative bar graph plot of diffusive and capacitive contributions under different scan rates of 5-100 mVs^{-1} is shown in Fig. 4K. Clearly, it was observed that the fraction of capacitive percent gradually increases from 10.7% to 34.5% with the increase in scan rate, while the diffusive percent decreases from 89.3% to 65.5%. The trend based on the scan rate indicates that at a low scan rate, the $Co_{0.75}Ni_{0.25}Te$/NF electrode was given enough time to undergo Faradic redox transitions, favouring a higher diffusion percentage in total performance. With the elevation of the scan rate from 5 to 100 mV s^{-1}, some of the electrode ions preferred to adsorb physically at the electrode/electrolyte interface, contributing to a higher capacitive percentage. However, for every scan rate test, a higher fraction of diffusive contribution as compared to capacitive contribution was obtained, which signifies the fast reversible redox transition and rate independent property of the $Co_{0.75}Ni_{0.25}Te$/NF electrode.

3.1.2. Two-electrode testing

Considering the excellent electrochemical performance and Faradaic storage characteristics of $Co_{0.75}Ni_{0.25}Te$/NF, an HSC assembly of $Co_{0.75}Ni_{0.25}Te$/NF with commercially available AC was fabricated as the positive and negative electrodes, respectively, in 2M KOH electrolyte. The detailed preparation and electrochemical testing of AC on NF are discussed in SI, Section 9. The schematic is illustrated in Fig. 5A. The association of battery-type and EDLC-type electrodes would explore their applicability in real-time energy storage applications. All the electrochemical testing details for the AC have been given in Fig. S6. Fig. 5B displays that the AC and $Co_{0.75}Ni_{0.25}Te$/NF are working in two different potential ranges; the AC in the negative potential window (0 to -1 V) and the $Co_{0.75}Ni_{0.25}Te$/NF in the positive potential window (0 to 0.5 V). Based on this, the overall working voltage window of the $Co_{0.75}Ni_{0.25}Te$/NF//AC assembly can be extended to 1.5 V. The mass balancing of the corresponding two electrodes was done using eqn (16), in which C is the specific capacity, ΔV is the potential window, and m is the mass of the electrode material, with respect to which a mass of 1.1 mg was chosen for AC.[71]

$$\frac{m_+}{m_-} = \frac{C^- \Delta V^-}{C_m^+ \Delta V^+} \qquad (16)$$

Fig. 5C-D illustrates the optimization of the working voltage window from 1 V to 1.5 V for the $Co_{0.75}Ni_{0.25}Te$/NF//AC by CV and GCD analysis at a scan rate of 100 mV s^{-1} and a current density of 5 mA cm^{-2}, respectively. As expected, the original shape of the CV and GCD curves did not show any distortion until 1.5 V. So, a voltage window of 1.5 V was implemented for further electrochemical analysis of the HSC assembly. The CV curve for $Co_{0.75}Ni_{0.25}Te$/NF//AC was recorded by varying the scan rate from 0 to 100 mV s^{-1}, as shown in Fig. 5E. Apparently, the CV performance indicates the amalgamation of two different

electrode behaviours: an EDLC-type and a battery-type electrode. In particular, at a lower voltage window, a low current response was obtained, which is because of the EDLC-based behaviour, while at a higher potential, a high current response corresponds to a rapid Faradaic reaction owing to the characteristics of battery type material. A persistent shape of the CV curve at various scan rates and a high amplitude in the current response from the zero current baseline indicate a good capacitive characteristic of the $Co_{0.75}Ni_{0.25}Te$/NF//AC HSC assembly.

The GCD analysis for $Co_{0.75}Ni_{0.25}Te$/NF//AC was performed under different current densities (0.8 to 4 mA cm^{-2}) and is represented in Fig. 5F. A plot of areal capacity and specific capacity with respect to various current densities is shown in Fig. 5G. The areal capacities of the HSC $Co_{0.75}Ni_{0.25}Te$//AC assembly electrode are 77.9, 70.1, 59.8, 54.7, 49.0, and 46.1 μAh cm^{-2} corresponding to the current densities of 0.8, 0.9, 1, 2, 3, and 4 mA cm^{-2}, respectively. Based on the mass deposition, the specific capacity values of the $Co_{0.75}Ni_{0.25}Te$//AC HSC are 67.7, 60.9, 52.0, 47.5, 42.6, and 40.0 mAh g^{-1} at the current densities of 0.8, 0.9, 1, 2, 3, and 4 mA cm^{-2}. High energy density, power density, and long-term stability are the key requirements for $Co_{0.75}Ni_{0.25}Te$/NF//AC to be established for practical applications. From the GCD curves, the energy density and power density of $Co_{0.75}Ni_{0.25}Te$/NF//AC were calculated using eqns (2) and (3).

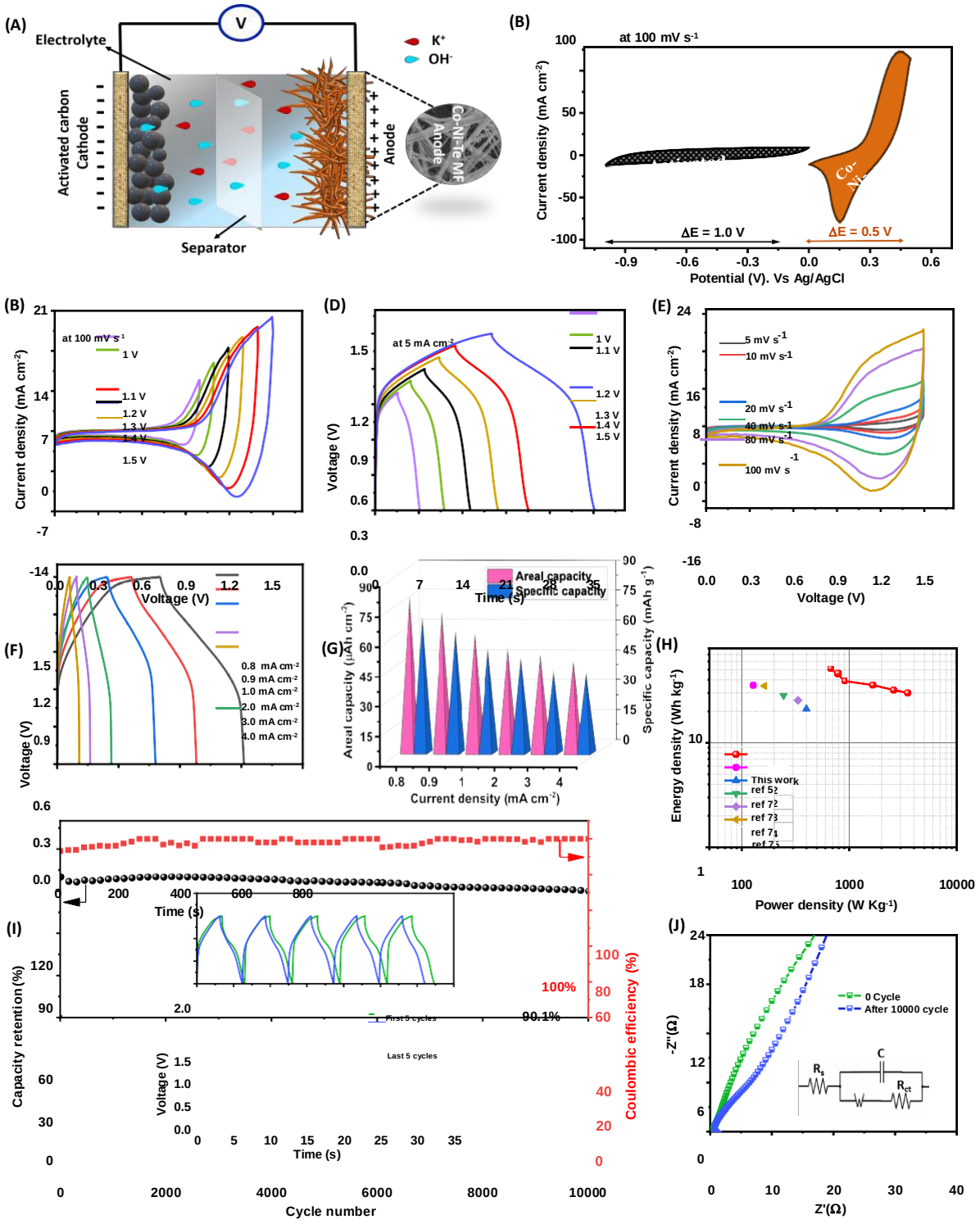

671

672 **Fig. 5.** (A) Illustration of HSC assembly of AC and $Co_{0.75}Ni_{0.25}Te$/NF. (B) CV curves of AC
673 and $Co_{0.75}Ni_{0.25}Te$/NF, respectively, obtained at a scan rate of 100 mV s^{-1}.Optimization of the
674 voltage window from 1 V to 1.5 V in (C) CV, and (D) GCD analysis, (E) CV curves at various
675 scan rates, (F) GCD curves at various current density, (G) areal capacity and specific capacity

vs. current density, (H) Ragone plot, (I) cyclic stability of $Co_{0.75}Ni_{0.25}Te$/NF//AC for 10,000 cycles, and (J) EIS Nyquist curve of $Co_{0.75}Ni_{0.25}Te$/NF//AC with equivalent circuit.

The Ragone plot (energy density vs. power density) with respect to different current densities is shown in Fig. 5H, along with a comparison of recently reported similar works. The assembled $Co_{0.75}Ni_{0.25}Te$/NF//AC delivered the highest energy density of 50.8 Wh kg^{-1} (58.4 μWh cm^{-2}) at a power density of 672.7 W kg^{-1} (773.5 μW cm^{-2}), which was comparatively high as compared to other similar reported materials.[52, 72-75] Even at a high-power density of 3498.1 W kg^{-1} (4019.4 μW cm^{-2}), an energy density of 30.0 Wh kg^{-1} (34.5 μWh cm^{-2}) was still maintained. Overall, the results validate that $Co_{0.75}Ni_{0.25}Te$/NF//AC all in one is an excellent electrode choice for supercapacitor applications.

The cyclic stability test of $Co_{0.75}Ni_{0.25}Te$/NF//AC for 10,000 cycles was done at a constant current density of 10 mA cm^{-2}. Fig. 5I shows the cyclic stability and coulombic efficiency of the HSC assembly. The cell activates for the first 2000 cycles; therefore, there is a rise in capacity during the initial cycles, and then its capacity value starts decaying gradually with the increase in cycle number. The compact packing and well-established electrode contact assembly of $Co_{0.75}Ni_{0.25}Te$/NF//AC resulted an excellent capacity retention of 90.1% and 100% columbic efficiency even after 10,000 successive cycles. Table ST3 of SI summarizes a comparison study of $Co_{0.75}Ni_{0.25}Te$/NF//AC with other recently reported Ni and Co chalcogenide-based electrodes. The obtained energy density values and stability for the assembled $Co_{0.75}Ni_{0.25}Te$/NF//AC were substantially higher than those reported for Ni and Co chalcogenide-based electrodes.

An EIS plot was collected for $Co_{0.75}Ni_{0.25}Te$/NF//AC before and after the stability test. $Co_{0.75}Ni_{0.25}Te$/NF//AC Nyquist plot with an equivalent circuit is presented in Fig. 5J, and Fig. S7 provides the fitted curve. From the plot, the R_s and R_{ct} values obtained before stability are 0.55 and 0.46 Ω, respectively, and even after the stability test, the R_s value was considerably

near, i.e., 0.81, however, the R_{ct} value increases to 6.05 Ω. After passing a stability test, the $Co_{0.75}Ni_{0.25}Te$ electrode was examined using FESEM, EDS, TEM, XRD, and XPS investigations in order to examine structural variation and the electrochemical reaction energy storage mechanism. According to the analysis, there haven't been many noticeable changes to the morphology, crystal structure, or valence state. Although the MF became a little agglomerated (Fig. S8A), the initial 1D fibril structure was still intact, indicating the excellent structural stability of synthesized $Co_{0.75}Ni_{0.25}Te$. Moreover, EDS analysis (Fig. S8B) confirms the presence of Co, Ni, and Te elements along with O and K, which may arise because of the residual KOH electrolyte interaction during the analysis. The TEM image of the $Co_{0.75}Ni_{0.25}Te$ electrode after 10,000 cycles given in Fig. S8C shows similar results as obtained in FESEM analysis. The XRD pattern obtained for the $Co_{0.75}Ni_{0.25}Te$ electrode after 10,000 cycles shows the stability of its hexagonal crystal structure (ICDD nos. 00-034-0420 (CoTe) and 00-038-1393 (NiTe)), where there is no peak shift observed from its 0^{th} cycle XRD pattern (Fig. S8D). An additional peak of K was obtained, which is because of residual KOH electrolyte from electrochemical performance matching the ICDD no.00-001-0500 of K. The XPS analysis of the $Co_{0.75}Ni_{0.25}Te$ after stability is given in Fig. S8E-G also confirms the almost same oxidation state of all three elements due to the reversible redox transition. Nevertheless, there was some peak broadening, which is a normal occurrence after such a lengthy stability test and is also due to the presence of residual intermediate states of CoTe and NiTe after redox transition. A strong, stable crystallinity, composition, and morphology obtained from $Co_{0.75}Ni_{0.25}Te$ indicate its suitability for real-time energy storage applications.

Finally, as demonstrated in Fig. 6A, the applicability of the $Co_{0.75}Ni_{0.25}Te$/NF//AC device for real-time application was tested by connecting two devices (4 cm^2) in series and charging them to 3 V for illuminating the red LED bulb. Fig. 6B shows the CV curve for single and two

serially connected devices at a scan rate of 100 mV s^{-1}. This confirms the voltage window can be elongated twice of what obtained from a single device. The optical figure in Fig. 6C indicates the serially connected device successfully illuminates the red LED bulb. With gradual consumption of current, the brightness of the bulb dims (Fig. 6D). The red bulb lit up very brightly and went out after 75 s. The video of the illumination of an LED bulb powered by two serially connected supercapacitor devices for 75 s is shown in Section 13. All the results definitely insights the promising potential of assembled $Co_{0.75}Ni_{0.25}Te$/NF//AC for future energy storage applications.

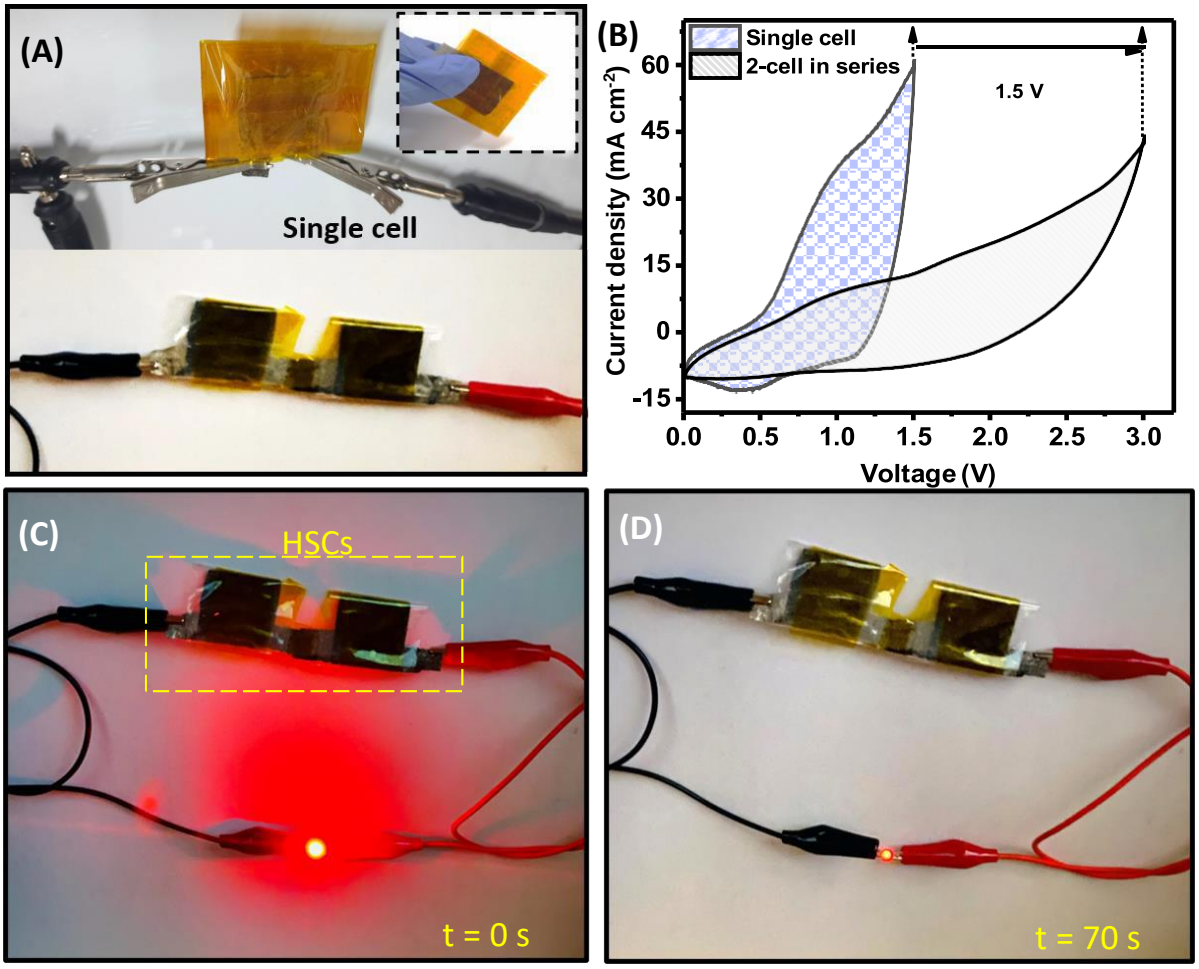

Fig. 6. (A) Optical image of experimental setup for single and 2-cell connected in series, (B) CV curve obtained for single and 2 cell connected in serial at 100 mV s^{-1}, optical photograph of LED bulb lighting (C) at t = 0 s, and (D) at t = 70 s.

3.1.3. OER activity of $Co_{0.75}Ni_{0.25}Te$/NF

The OER catalytic activity of the $Co_xNi_{(1-x)}Te$/NF was investigated in 0.1 M KOH aqueous electrolyte in the standard three-electrode system at a scan rate of 5 mV s^{-1} in the working window of -0.1 to 0.6 V vs. RHE. For comparison, bare NF and commercial RuO_2 were tested along with all the optimized $Co_xNi_{(1-x)}Te$/NF under similar conditions. Fig. 7A shows the auto iR (internal resistance) compensated linear scan voltammetry (LSV) plots for $Co_{1.00}Ni_{0.00}Te$/NF, $Co_{0.75}Ni_{0.25}Te$/NF, $Co_{0.50}Ni_{0.50}Te$/NF, $Co_{0.25}Ni_{0.75}Te$/NF, and $Co_{0.00}Ni_{1.00}Te$/NF, RuO_2, and bare NF at a scan rate of 5 mV s^{-1}. Commercial RuO_2 was coated on NF using a slurry coating technique, and the details of electrode preparation are mentioned in Section 14 of SI. The OER performance of $Co_{0.75}Ni_{0.25}Te$/NF was much better as compared to all optimized electrodes, bare NF, and the commercial benchmark catalyst, RuO_2. In detail, $Co_{0.75}Ni_{0.25}Te$ only requires an η of 289 mV to reach the current density (j) of 10 mA cm^{-2}, while $Co_{1.00}Ni_{0.00}Te$/NF, $Co_{0.50}Ni_{0.50}Te$/NF, $Co_{0.25}Ni_{0.75}Te$/NF, $Co_{0.00}Ni_{1.00}Te$/NF, commercial RuO_2, and bare NF showed a low current response and a higher water oxidation η of 328, 344, 339, 398, 395, and 291 mV, respectively, at a current density of 10 mA cm^{-2}. Also, compared to other optimised electrodes, $Co_{0.75}Ni_{0.25}Te$ exhibits a high current density of 60 mA cm^{-2} at a constant overpotential of 0.4 V vs. RHE, which means that its oxygen evolution rate is higher.[76] For in-depth determination of the OER kinetic mechanism, the Tafel slopes of the catalysts were obtained from the plot of η vs. log(j), as shown in Fig. 7B. The OER catalytic activity of different optimized electrodes followed the same trend as that observed in the case of supercapacitor applications. The Tafel slopes obtained for $Co_{1.00}Ni_{0.00}Te$/NF, $Co_{0.75}Ni_{0.25}Te$/NF, $Co_{0.50}Ni_{0.50}Te$/NF, $Co_{0.25}Ni_{0.75}Te$/NF, $Co_{0.00}Ni_{1.00}Te$/NF, RuO_2, and bare NF were 197, 102, 117, 136, 180, 127, and 221 mV dec^{-1}, respectively. The Tafel slope value decreases until the (3:1) ratio of Co/Ni ($Co_{0.75}Ni_{0.25}Te$/NF) and then gradually increases with the increase of Ni content, ensuring $Co_{0.75}Ni_{0.25}Te$/NF possesses the fastest OER kinetics. The

$Co_{0.75}Ni_{0.25}Te$/NF Tafel value demonstrates that the rate-determining step is at the termination of the multiple electron transfer reaction mechanism.[77] The significantly lower η and Tafel slope value for $Co_{0.75}Ni_{0.25}Te$ as compared to all optimized electrodes, bare NF, and RuO_2, demonstrates its excellent OER catalytic behaviour. Fig. 7C shows the comparison of η and Tafel slope values for $Co_{0.75}Ni_{0.25}Te$/NF, commercial RuO_2, and bare NF, among which $Co_{0.75}Ni_{0.25}Te$/NF excels in both of the values.

The EIS measurement was carried out with respect to applied η vs. Ag/AgCl at a frequency range of 0.1 Hz to 100 kHz (Fig. 7D). The fitted equivalent circuit with respect to optimized electrode material is given in Fig. S9A-C, and the corresponding R_s and R_{ct} values are summarised in Fig. S9D. From the EIS curves, it is quite evident all optimized $Co_xNi_{(1-x)}Te$/NF electrodes showed similar curve characteristics, the R_{ct} value obtained for $Co_{0.75}Ni_{0.25}Te$ MF is smaller, i.e., 1.02 Ω, as compared to $Co_{1.00}Ni_{0.00}Te$/NF (1.51 Ω), $Co_{0.50}Ni_{0.50}Te$/NF (1.21 Ω), $Co_{0.25}Ni_{0.75}Te$/NF (1.63 Ω), $Co_{0.00}Ni_{1.00}Te$/NF (1.12 Ω), bare NF (21.94 Ω) and much smaller than RuO_2 (12.98 Ω) indicating higher conductivity of $Co_{0.75}Ni_{0.25}Te$ MF. The excellent OER performance of $Co_{0.75}Ni_{0.25}Te$ MF at low concentration electrolyte, i.e., 0.1 M KOH, was achieved because of the homogenous in-situ growth of fibril networks on the NF, which provides a high electrochemical surface area and evades the use of any binder, thus providing improved ion kinetics.[77] Moreover, benefiting from the synergistic effect of conductive Te and multi-metal Co and Ni, they offer low charge transfer resistance and efficient electron transport between catalyst and substrate.

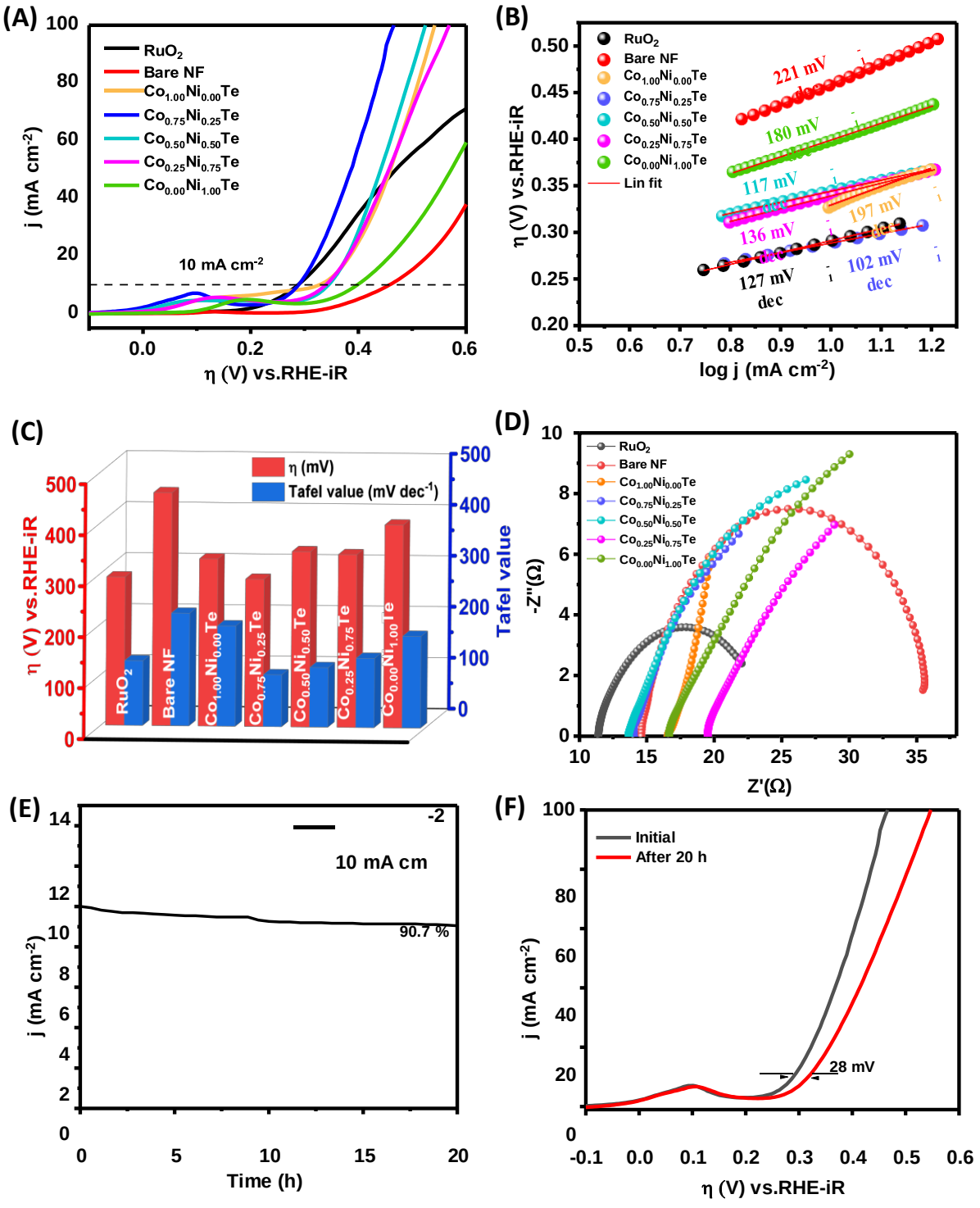

788

789 **Fig. 7.** Electrocatalytic testing: (A) LSV curves, (B) Tafel plots (η vs. log(j)), (C) comparison

790 of η and Tafel slope value, and (D) EIS curve of all optimized $Co_xNi_{(1-x)}Te$/NF electrocatalysts,

791 commercial RuO_2 and bare NF, (E) Chronopotentiometric curve of $Co_{0.75}Ni_{0.25}Te$/NF in 0.1 M

792 KOH electrolyte at constant current density of 10 mA cm^{-2}, and (F) LSV polarization curves

793 of initial and after 20 h at a voltage window of 0.6 V.

Another important requirement is the long-term stability of electrode catalysts for OER. Fig. 7E shows the stability test done for $Co_{0.75}Ni_{0.25}Te$ MF/NF at 10 mA cm^{-2} for continuous 20 h OER reactions. After 20 h of consecutive cycling, there was a slight decrease in the *j* value, but the efficiency remained at 90.7 %. Fig. 7F shows the before and after stability LSV plots, which show there is a small declination of the η value, i.e., 28 mV, from its initial cycle, confirming its excellent catalytic stability. After the stability test, the material was characterized by FESEM EDS, TEM, and XRD analyses, as shown in Fig. S10A-D. The long microfibril network of $Co_{0.75}Ni_{0.25}Te$ was still obtained, and no other damage was found even after 20 h of OER reactions, showing its excellent structural stability. EDS analysis shows the presence of Co, Ni, and Te elements along with K. The TEM image of the $Co_{0.75}Ni_{0.25}Te$ electrode after 20 h confirms the similar results observed during FESEM analysis. A comparative XRD pattern before and after 20 h analysis for the $Co_{0.75}Ni_{0.25}Te$ electrode reveals the stability of its hexagonal crystal structure. An additional peak of K was obtained from residual KOH electrolyte during electrochemical performance. Such good electrochemical and structural stability confirms the suitability of the electrode in OER applications. The comparative study of synthesized $Co_{0.75}Ni_{0.25}Te$ MF with other reported Ni/Co based water oxidation catalysts is listed in Table ST4, and it demonstrates its superiority over other reported Ni/Co based electrocatalysts.

To determine the number of active sites of the catalyst all optimized $Co_xNi_{(1-x)}Te$ MF and RuO_2, ECSA, and RF values were measured from C_{dl} evaluated by the non-Faradaic CV region for different scan rates by following eqns (5) and (6) respectively (Fig. S11A-F). The C_{dl}, ECSA and RF values are obtained from the slope plotted between capacitive current density vs. scan rates as shown in Fig. S11G, and the values are summarized in Fig. S11H. $Co_{0.75}Ni_{0.25}Te$/NF displayed maximum C_{dl}, ECSA, and RF as compared to all optimized Co/Ni ratios, i.e., 6.26

mF cm^{-2}, 156.50 cm^2, and 391.25 respectively. Even though these values were much lower than the C_{dl}, ECSA, and RF values of RuO_2, i.e., 13.74 mF cm^{-2}, 343.50 cm^2 and 858.75, respectively. The overall catalytic performance was in favour of $Co_{0.75}Ni_{0.25}Te$ MF as compared to other optimized electrodes because of its higher conductivity and stable, long microfibril network associated with the multielement synergistic effect of $Co_{0.75}Ni_{0.25}Te$.

3.2. Theoretical study using density functional theory (DFT)

The model structure considered for the study is shown in Fig. 8A. To estimate the quantum capacitance, the density of states is computed for three compositions, $Co_{0.75}Ni_{0.25}Te$, $Co_{0.50}Ni_{0.50}Te$, and $Co_{0.25}Ni_{0.75}Te$ (Fig. 8B, C, and D). Quantum capacitance is calculated using the following formula:

$$C_Q = e^2 \int_{-\infty}^{+\infty} D(E) F_T(E\text{-}e\varphi)\, dE \quad (17)$$

Where, D(E) and φ represent the density of states and electrode potential of the given system, respectively. $F_T(E)$ stands for the thermal broadening function due to the thermal effect, which is estimated using the following equation:

$$F_T(E) = (4KT)^{-1} \operatorname{sech}^2(E/2KT) \quad (18)$$

Here, K and T represent Boltzmann's constant and temperature, taken as 300 K. Quantum capacitance values calculated for three compositions are shown in Fig. 8E.

To calculate the quantum capacitance of the material the (101) plane was chosen since in the experimental XRD analysis the intensity peak along (101) plane is higher than the peaks observed along other different planes. Hence, the higher number of atoms of the system considered are oriented along this direction i.e., along (101) plane. The quantum capacitance of composition $Co_{0.75}Ni_{0.25}Te$ for two different planes (101) and (001) was also computed as

shown in Fig. S12. And it is clear that the obtained quantum capacitance value is found to be higher for (101) plane than (001).

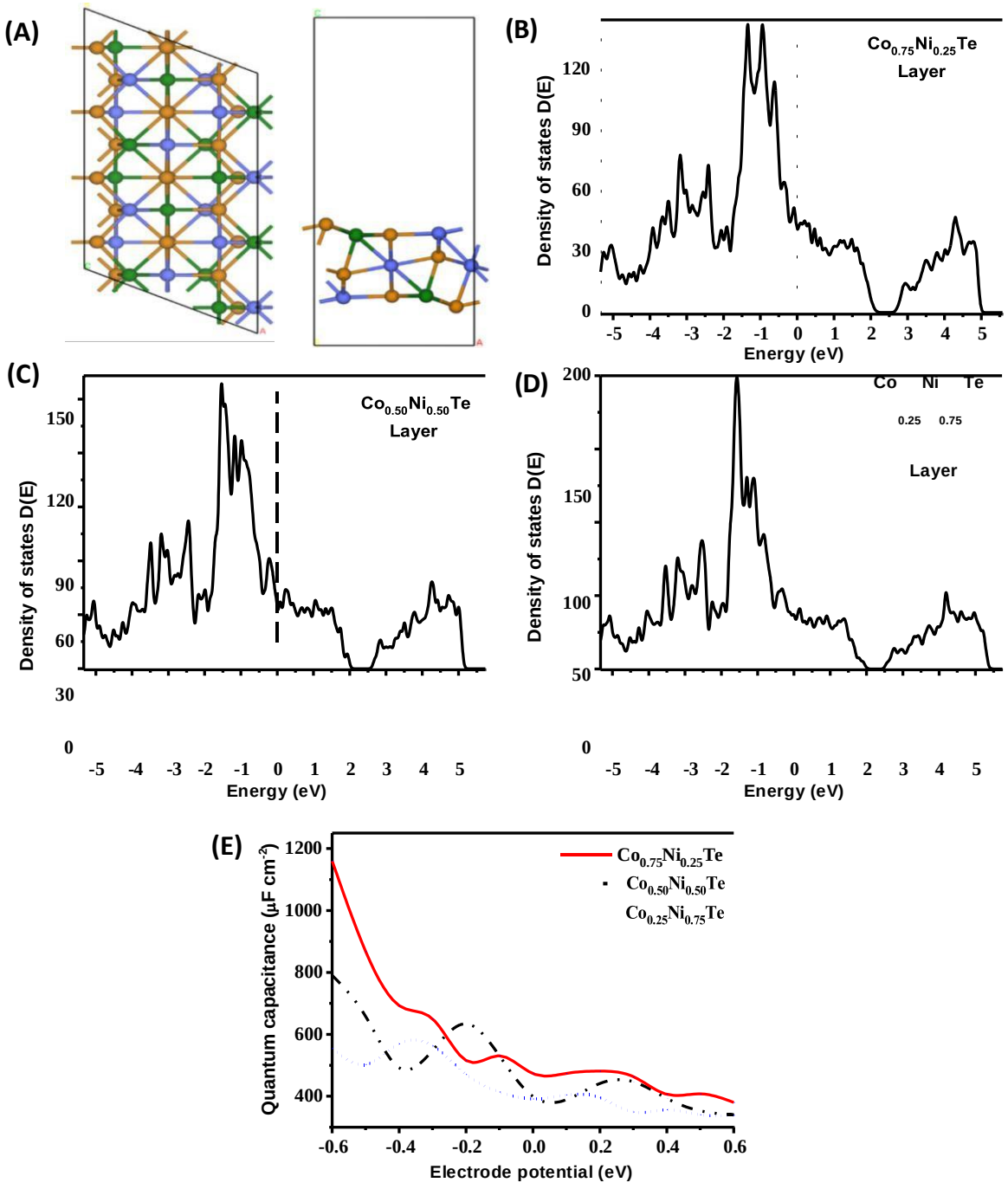

Fig. 8. (A) Top and side views of the supercell model structure of $Co_{0.75}Ni_{0.25}Te$ cleaved on 101 plane. Blue, green, and brown coloured spheres represent the Co, Ni, and Te atoms, respectively. Density of state plots of (B) $Co_{0.75}Ni_{0.25}Te$, (C) $Co_{0.50}Ni_{0.50}Te$, and (D) $Co_{0.25}Ni_{0.75}Te$. (E) Quantum capacitance plots for varying electrode potentials for compositions

851 $Co_{0.75}Ni_{0.25}Te$, $Co_{0.50}Ni_{0.50}Te$, and $Co_{0.25}Ni_{0.75}Te$.

852

For $Co_{0.75}Ni_{0.25}Te$, the maximum and minimum values of quantum capacitance are estimated to be 1160 µF cm^{-2} at -0.6 V and 380 µF cm^{-2} at 0.6 V, respectively. For $Co_{0.5}Ni_{0.5}Te$, the maximum quantum capacitance value is at the applied voltage of -0.6 V, or 790 µF cm^{-2} and the minimum is 340 µF cm^{-2} at 0.6 V. And for $Co_{0.25}Ni_{0.75}Te$, the maximum 569 µF cm^{-2} and the minimum 338 µF cm^{-2} values of quantum capacitance are found at -0.4 V and at 0.6 V, respectively. The results prove that the $Co_{0.75}Ni_{0.25}Te$ composition is better than the $Co_{0.50}Ni_{0.50}Te$ and $Co_{0.25}Ni_{0.75}Te$ compositions for quantum capacitance, which is due to the enhanced density of states near the Fermi level.[78, 79]

Experimental analyses show the presence of OH during the catalytic reaction process. So, two cases of OH coverage are considered for the theoretical OER activity study, as shown in Fig. S13. Firstly, the OH molecule's adsorption energy on the Co, Ni, and Te is estimated, and OH has high adsorption on Co atom. The binding energies of the OH molecule on the Co, Ni, and Te atoms are -3.62 eV, -3.05 eV, and -2.93 eV, respectively (Fig. S14). Also, it is well known that among the transition metals, Co shows high OER activity.[80, 81] So, Co-atom as an active site with two OH coverages (considering a total of 8 atoms including Co and Ni, one adsorbed OH, i.e., 1/8 = 0.125, and three adsorbed OH, i.e., 3/8 = 0.375) on the surface is considered for estimating the OER activity. The OER activity with Ni as an active site is also estimated under 0.375 OH coverage (Fig. S15). Even under high coverage, the overpotential is high at 1.14 V, thereby proving Ni is not an active site. The OER activity is estimated using the following free energy equations under alkaline conditions:

$$\Delta G1 = * + 4OH^- \rightarrow OH^* + 3OH^- + e^- \quad (19)$$

$$\Delta G2 = OH^* + 3OH^- + e^- \rightarrow O^* + H_2O + 2OH^- + 2e^- \quad (20)$$

$$\Delta G3 = O^* + 2OH^- + H_2O + 2e^- \rightarrow OOH^* + H_2O + OH^- + 3e^- \quad (21)$$

878 $\Delta G4 = OOH^* + H_2O + OH^- + 3e^- \rightarrow O_2 + 2H_2O + 4e^-$ (22)

879

880 Here, * represents the active site on the surface. For 0.125 OH coverage, two Co atoms, Co1
881 and Co2, are taken as active sites. Co1 has Co-atoms as its nearest neighbours, while Co2 has
882 Ni-atoms. The structure models and free energy plots are given in Fig. 9A-Ai-C-Ci. From the
883 plots, the overpotential on Co1 is $\eta = 1.46$ V, and on Co2 it is $\eta = 1.58$ V. These overpotentials
884 are very high, thereby proving that at 0.125 OH coverage, the surface is not efficient for OER.
885 Free energy is estimated on Co3 as an active site for 0.375 OH coverage (to be noted that the
886 OH molecules are fixed to prevent them from interacting with each other when estimating the
887 free energies).

888

889 The overpotential is significantly reduced to $\eta = 0.76$ V. Out of four possible potential
890 determining steps (PDS) (red-coloured numbers in Fig. 9A), the 3rd step, i.e., ΔG_O to ΔG_{OOH},
891 is the PDS. This shows strong O* interaction with the surface, and its role in determining the
892 PDS is well explained by Samadhan et al. [82]. Also, only in this case, the O* intermediate
893 binds in enolate form, unlike in the other two cases (Fig. 9C). Further, the d-band center of the
894 active sites is calculated as it is a known catalytic descriptor for transition metals [83]. When
895 the OH coverage is increased, the d-band center becomes more negative with respect to the
896 Fermi level, which would reduce the O* intermediate binding, thereby reducing the
897 overpotential as well (d-band for sites Co1, Co2, and Co3 are -1.41 eV, -1.49 eV, and -1.59
898 eV, respectively, shown in Fig. S16. This shows that increased OH coverage helps in reducing
899 the otherwise high O* binding on the Ni neighboured Co site, which increases OER efficiency.
900 These findings unequivocally support the hypothesis that produced $Co_{0.75}Ni_{0.25}Te$/NF
901 bifunctional electrode has enormous potential to meet the current need for energy storage and
902 electrocatalytic application in our daily needs.

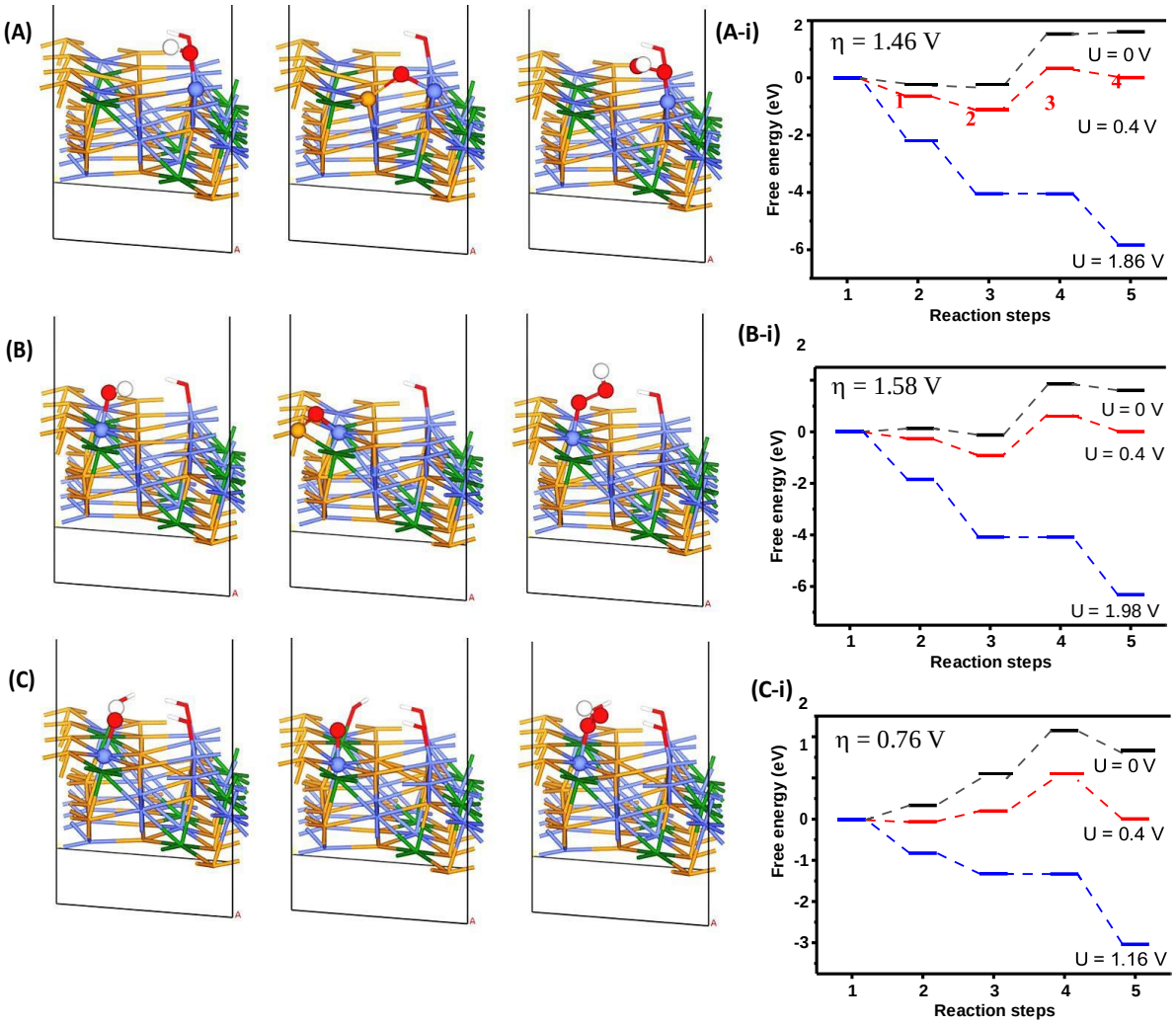

903

904 **Fig. 9.** Structure models showing adsorbed intermediates of OER (OH*, O*, and OOH*) on

905 active sites and corresponding free energy plots for OER activity on $Co_{0.75}Ni_{0.25}Te$ surface on
906 active sites (A, A-i) Co1, (B, B-i) Co2, and (C, C-i) Co3, respectively. Adsorbates and
907 corresponding active site atoms are represented as spheres, rest of the atoms are indicated in
908 line and stick models. The colours of the spheres/sticks are the same as represented in previous
909 the Figures.

910

911 **4. Conclusions**

912 In this paper, an oven-based wet chemical method was adapted for synthesizing
913 $Co_xNi_{(1-x)}Te$ MFs on NF and shows enhanced activity for both supercapacitor and OER
914 activity. It was observed that based on various Co/Ni ratios reactivity with Te, $Co_xNi_{(1-x)}Te$

915 MFs/NF displayed morphological alteration and variable electrochemical behavior.

Electrochemical tests revealed $Co_{0.75}Ni_{0.25}Te$/NF to be the best performing electrode as compared to other optimized electrodes. At this particular composition, the inheritance of high theoretical capacitance of Ni-based compounds, along with the perfect microfibril network on NF, helps achieve the highest electrochemical performance. Moreover, conductive telluride and synergistic effects from Co, Ni, and Te help in enhancing the electrochemical performance. The $Co_{0.75}Ni_{0.25}Te$/NF achieved a maximum areal capacity of 188.9 μAh cm^{-2} (157.4 mAh g^{-1}) at a current density of 0.8 mA cm^{-2} in a three-electrode system. Additionally, an HSC assembly of $Co_{0.75}Ni_{0.25}Te$/NF with AC was fabricated, from which a maximum areal capacity of 77.9 μAh cm^{-2} (67.7 mAh g^{-1}) at a current density of 0.8 mA cm^{-2} was obtained. The assembled two-electrode system reaches the highest energy density of 50.8 Wh kg^{-1} (58.4 μWh cm^{-2}) at a power density of 672.7 W kg^{-1} (773.5 μW cm^{-2}), and an outstanding stability of up to 10,000 cycles with capacity retention of 90.1% was achieved. As an electrocatalyst, $Co_{0.75}Ni_{0.25}Te$ MF/NF only required a low η of 289 mV to reach a current density of 10 mA cm^{-2} with a Tafel slope of 102 mV dec^{-1} in 0.1 M KOH for OER. Further, a DFT study of the composition $Co_{0.75}Ni_{0.25}Te$ shows better quantum capacitance due to the increased density of states near Fermi levels, and this composition ratio also shows better OER activity with increasing OH coverage. The outcomes surely highlight the potential of $Co_{0.75}Ni_{0.25}Te$ MF as an electrode for future real-time energy storage and conversion applications.

Declaration

The authors declare that they have no known financial or interpersonal conflicts that would have appeared to have an impact on the research presented in this study.

Acknowledgments

P.B. and A.K.S. are grateful to SERB, New Delhi, India (CRG/2018/003533) for the financial support, as well as the Karnataka Science and Technology Promotion Society (KSTePS/VGST-RGS-F/2018-19/GRD No.831/315). The authors express their gratitude to the CNMS, Jain University, for FESEM facility.

References

[1] M. Karnan, K. Subramani, P. Srividhya, M. Sathish, Electrochemical studies on corncob derived activated porous carbon for supercapacitors application in aqueous and non-aqueous electrolytes, Electrochimica Acta 228 (2017) 586-596.

[2] T. Kshetri, T.I. Singh, Y.S. Lee, D.D. Khumujam, N.H. Kim, J.H. Lee, Metal organic framework-derived cobalt telluride-carbon porous structured composites for high-performance supercapacitor, Composites Part B: Engineering 211 (2021) 108624. https://doi.org/https://doi.org/10.1016/j.compositesb.2021.108624.

[3] X. Chen, C. Li, M. Grätzel, R. Kostecki, S.S. Mao, Nanomaterials for renewable energy production and storage, Chemical Society Reviews 41(23) (2012) 7909-7937. https://doi.org/10.1039/C2CS35230C.

[4] S. Hatfield-Dodds, H. Schandl, D. Newth, M. Obersteiner, Y. Cai, T. Baynes, J. West, P. Havlik, Assessing global resource use and greenhouse emissions to 2050, with ambitious resource efficiency and climate mitigation policies, Journal of Cleaner Production 144 (2017) 403-414. https://doi.org/https://doi.org/10.1016/j.jclepro.2016.12.170.

[5] U. Gupta, C.N.R. Rao, Hydrogen generation by water splitting using MoS2 and other transition metal dichalcogenides, Nano Energy 41 (2017) 49-65. https://doi.org/https://doi.org/10.1016/j.nanoen.2017.08.021.

963 [6] Z. Wang, H. Liu, R. Ge, X. Ren, J. Ren, D. Yang, L. Zhang, X. Sun, Phosphorus-Doped
964 Co3O4 Nanowire Array: A Highly Efficient Bifunctional Electrocatalyst for Overall Water
965 Splitting, ACS Catalysis 8(3) (2018) 2236-2241. https://doi.org/10.1021/acscatal.7b03594.
966 [7] X. Zhang, J. Li, Y. Yang, S. Zhang, H. Zhu, X. Zhu, H. Xing, Y. Zhang, B. Huang, S. Guo,
967 E. Wang, Co3O4/Fe0.33Co0.66P Interface Nanowire for Enhancing Water Oxidation
968 Catalysis at High Current Density, Advanced Materials 30(45) (2018) 1803551.
969 https://doi.org/https://doi.org/10.1002/adma.201803551.
970 [8] X. Han, G. He, Y. He, J. Zhang, X. Zheng, L. Li, C. Zhong, W. Hu, Y. Deng, T.-Y. Ma,
971 Engineering Catalytic Active Sites on Cobalt Oxide Surface for Enhanced Oxygen
972 Electrocatalysis, Advanced Energy Materials 8(10) (2018) 1702222.
973 https://doi.org/https://doi.org/10.1002/aenm.201702222.
974 [9] Y. Zhang, H. Zhang, L. Fang, J. Deng, Y. Wang, Facile Synthesis of Nickel Manganese
975 Composite Oxide Nanomesh for Efficient Oxygen Evolution Reaction and Supercapacitors,
976 Electrochimica Acta 245 (2017) 32-40.
977 https://doi.org/https://doi.org/10.1016/j.electacta.2017.05.119.
978 [10] R.C. Rohit, A.D. Jagadale, S.K. Shinde, D.Y. Kim, V.S. Kumbhar, M. Nakayama,
979 Hierarchical nanosheets of ternary CoNiFe layered double hydroxide for supercapacitors and
980 oxygen evolution reaction, Journal of Alloys and Compounds 863 (2021) 158081.
981 https://doi.org/https://doi.org/10.1016/j.jallcom.2020.158081.
982 [11] B. Jansi Rani, S.S. Pradeepa, Z.M. Hasan, G. Ravi, R. Yuvakkumar, S.I. Hong,
983 Supercapacitor and OER activity of transition metal (Mo, Co, Cu) sulphides, Journal of Physics
984 and Chemistry of Solids 138 (2020) 109240.
985 https://doi.org/https://doi.org/10.1016/j.jpcs.2019.109240.
986 [12] S. Liu, K. San Hui, K.N. Hui, J.M. Yun, K.H. Kim, Vertically stacked bilayer
987 CuCo2O4/MnCo2O4 heterostructures on functionalized graphite paper for high-performance

electrochemical capacitors, Journal of Materials Chemistry A 4(21) (2016) 8061-8071. https://doi.org/10.1039/C6TA00960C.

[13] K. Xu, S. Ma, Y. Shen, Q. Ren, J. Yang, X. Chen, J. Hu, CuCo2O4 nanowire arrays wrapped in metal oxide nanosheets as hierarchical multicomponent electrodes for supercapacitors, Chemical Engineering Journal 369 (2019) 363-369. https://doi.org/https://doi.org/10.1016/j.cej.2019.03.079.

[14] F. Saleki, A. Mohammadi, S.E. Moosavifard, A. Hafizi, M.R. Rahimpour, MOF assistance synthesis of nanoporous double-shelled CuCo2O4 hollow spheres for hybrid supercapacitors, Journal of Colloid and Interface Science 556 (2019) 83-91. https://doi.org/https://doi.org/10.1016/j.jcis.2019.08.044.

[15] Y. Li, L. Cao, L. Qiao, M. Zhou, Y. Yang, P. Xiao, Y. Zhang, Ni–Co sulfide nanowires on nickel foam with ultrahigh capacitance for asymmetric supercapacitors, Journal of Materials Chemistry A 2(18) (2014) 6540-6548. https://doi.org/10.1039/C3TA15373H.

[16] J. Saddique, X. Cheng, H. Shi, R. Wu, Y. Zhang, High-Performance Ni-Co Sulfide Nanosheet-Nanotubes Grown on Ni Foam as a Binder Free Electrode for Supercapacitors, Applied Sciences 9(15) (2019) 3082.

[17] F. Yang, J. Yao, F. Liu, H. He, M. Zhou, P. Xiao, Y. Zhang, Ni–Co oxides nanowire arrays grown on ordered TiO2 nanotubes with high performance in supercapacitors, Journal of Materials Chemistry A 1(3) (2013) 594-601. https://doi.org/10.1039/C2TA00055E.

[18] H. Wang, Q. Gao, L. Jiang, Facile Approach to Prepare Nickel Cobaltite Nanowire Materials for Supercapacitors, Small 7(17) (2011) 2454-2459. https://doi.org/https://doi.org/10.1002/smll.201100534.

[19] Z. He, Y. Yang, J.-W. Liu, S.-H. Yu, Emerging tellurium nanostructures: controllable synthesis and their applications, Chemical Society Reviews 46(10) (2017) 2732-2753. https://doi.org/10.1039/C7CS00013H.

[20] P. Bhol, S. Swain, A. Altaee, M. Saxena, A. Samal, Cobalt–iron decorated tellurium nanotubes for high energy density supercapacitor, Materials Today Chemistry 24 (2022) 100871.

[21] E.-K. Kim, H.T. Bui, N.K. Shrestha, C.Y. Shin, S.A. Patil, S. Khadtare, C. Bathula, Y.-Y. Noh, S.-H. Han, An enhanced electrochemical energy conversion behavior of thermally treated thin film of 1-dimensional CoTe synthesized from aqueous solution at room temperature, Electrochimica Acta 260 (2018) 365-371. https://doi.org/https://doi.org/10.1016/j.electacta.2017.12.072.

[22] Q. Qin, G. Zhang, Z. Chai, J. Zhang, Y. Cui, T. Li, W. Zheng, Ionic liquid-assisted synthesis of Cu7Te4 ultrathin nanosheets with enhanced electrocatalytic activity for water oxidation, Nano Energy 41 (2017) 780-787. https://doi.org/https://doi.org/10.1016/j.nanoen.2017.03.009.

[23] M. Manikandan, K. Subramani, M. Sathish, S. Dhanuskodi, NiTe Nanorods as Electrode Material for High Performance Supercapacitor Applications, ChemistrySelect 3(31) (2018) 9034-9040. https://doi.org/https://doi.org/10.1002/slct.201801421.

[24] L.K. Bommineedi, T.K. Shivasharma, B.R. Sankapal, Mixed phase FeTe: Fe2TeO5 nanopebbles through solution chemistry: Electrochemical supercapacitor application, Ceramics International 48(1) (2022) 137-147. https://doi.org/https://doi.org/10.1016/j.ceramint.2021.09.089.

[25] P. Zhou, L. Fan, J. Wu, C. Gong, J. Zhang, Y. Tu, Facile hydrothermal synthesis of NiTe and its application as positive electrode material for asymmetric supercapacitor, Journal of Alloys and Compounds 685 (2016) 384-390. https://doi.org/https://doi.org/10.1016/j.jallcom.2016.05.287.

[26] B. Ye, C. Gong, M. Huang, Y. Tu, X. Zheng, L. Fan, J. Lin, J. Wu, Improved performance of a CoTe//AC asymmetric supercapacitor using a redox additive aqueous electrolyte, RSC Advances 8 (2018) 7997-8006. https://doi.org/10.1039/c7ra12919j.

[27] S.J. Patil, B.H. Patil, R.N. Bulakhe, C.D. Lokhande, Electrochemical performance of a portable asymmetric supercapacitor device based on cinnamon-like La2Te3 prepared by a chemical synthesis route, RSC Advances 4(99) (2014) 56332-56341. https://doi.org/10.1039/C4RA09124H.

[28] Z. Chen, M. Chen, X. Yan, H. Jia, B. Fei, Y. Ha, H. Qing, H. Yang, M. Liu, R. Wu, Vacancy Occupation-Driven Polymorphic Transformation in Cobalt Ditelluride for Boosted Oxygen Evolution Reaction, ACS Nano 14(6) (2020) 6968-6979. https://doi.org/10.1021/acsnano.0c01456.

[29] A. Hassan, L. Nisar, R. Iqbal, M. Sadaqat, F. Hussain, M.N. Ashiq, M. Najam-ul-Haq, A. Shah, K.S. Joya, Copper telluride nanowires for high performance electrocatalytic water oxidation in alkaline media, Journal of Power Sources 491 (2021) 229628. https://doi.org/https://doi.org/10.1016/j.jpowsour.2021.229628.

[30] M. Manikandan, K. Subramani, S. Dhanuskodi, M. Sathish, One-Pot Hydrothermal Synthesis of Nickel Cobalt Telluride Nanorods for Hybrid Energy Storage Systems, Energy & Fuels 35(15) (2021) 12527-12537. https://doi.org/10.1021/acs.energyfuels.1c00351.

[31] S. Zhang, D. Yang, M. Zhang, Y. Liu, T. Xu, J. Yang, Z.-Z. Yu, Synthesis of novel bimetallic nickel cobalt telluride nanotubes on nickel foam for high-performance hybrid supercapacitors, Inorganic Chemistry Frontiers 7(2) (2020) 477-486. https://doi.org/10.1039/C9QI01395D.

[32] G. Qian, Y. Mo, C. Yu, H. Zhang, T. Yu, L. Luo, S. Yin, Free-standing bimetallic CoNiTe2 nanosheets as efficient catalysts with high stability at large current density for oxygen

evolution reaction, Renewable Energy 162 (2020) 2190-2196. https://doi.org/https://doi.org/10.1016/j.renene.2020.10.028.

[33] X. Yu, Z. Sun, Z. Yan, B. Xiang, X. Liu, P. Du, Direct growth of porous crystalline NiCo2O4 nanowire arrays on a conductive electrode for high-performance electrocatalytic water oxidation, Journal of Materials Chemistry A 2(48) (2014) 20823-20831. https://doi.org/10.1039/C4TA05315J.

[34] P. Bhol, S. Swain, S. Jena, K. Bhatte, C.S. Rout, M. Saxena, A.H. Jadhav, A.K. Samal, Co-Decorated Tellurium Nanotubes for Energy Storage Applications, ACS Applied Nano Materials 4(9) (2021) 9008-9021. https://doi.org/10.1021/acsanm.1c01613.

[35] S.C. Sekhar, G. Nagaraju, J.S. Yu, Conductive silver nanowires-fenced carbon cloth fibers-supported layered double hydroxide nanosheets as a flexible and binder-free electrode for high-performance asymmetric supercapacitors, Nano Energy 36 (2017) 58-67. https://doi.org/https://doi.org/10.1016/j.nanoen.2017.04.019.

[36] S. Huang, Y. Meng, S. He, A. Goswami, Q. Wu, J. Li, S. Tong, T. Asefa, M. Wu, N-, O-, and S-Tridoped Carbon-Encapsulated Co9S8 Nanomaterials: Efficient Bifunctional Electrocatalysts for Overall Water Splitting, Advanced Functional Materials 27(17) (2017) 1606585. https://doi.org/https://doi.org/10.1002/adfm.201606585.

[37] G. Kresse, J. Furthmüller, Efficiency of ab-initio total energy calculations for metals and semiconductors using a plane-wave basis set, Computational Materials Science 6(1) (1996) 15-50. https://doi.org/https://doi.org/10.1016/0927-0256(96)00008-0.

[38] J.P. Perdew, K. Burke, M. Ernzerhof, Generalized Gradient Approximation Made Simple, Physical Review Letters 77(18) (1996) 3865-3868. https://doi.org/10.1103/PhysRevLett.77.3865.

[39] J.J. Mortensen, L.B. Hansen, K.W. Jacobsen, Real-space grid implementation of the projector augmented wave method, Physical Review B 71(3) (2005) 035109. https://doi.org/10.1103/PhysRevB.71.035109.

[40] F. Neese, WIREs Comput. Mol. Sci. 2012, 2, 73; b) S. Grimme, J. Comput. Chem 27 (2006) 1787.

[41] W. Tang, E. Sanville, G. Henkelman, A grid-based Bader analysis algorithm without lattice bias, Journal of Physics: Condensed Matter 21(8) (2009) 084204. https://doi.org/10.1088/0953-8984/21/8/084204.

[42] J. Kang, S. Zhang, Z. Zhang, Three-Dimensional Binder-Free Nanoarchitectures for Advanced Pseudocapacitors, Advanced Materials 29(48) (2017) 1700515. https://doi.org/https://doi.org/10.1002/adma.201700515.

[43] Z. Yu, Z. Cheng, G. Tsekouras, X. Wang, X. Kong, M. Osada, S.X. Dou, High areal capacitance and rate capability using filled Ni foam current collector, Electrochimica Acta 281 (2018) 761-768. https://doi.org/https://doi.org/10.1016/j.electacta.2018.06.007.

[44] Y.-M. Wang, D.-D. Zhao, Y.-Q. Zhao, C.-L. Xu, H.-L. Li, Effect of electrodeposition temperature on the electrochemical performance of a Ni(OH)2electrode, RSC Advances 2 (2012) 1074-1082. https://doi.org/10.1039/c1ra00613d.

[45] G.-W. Yang, C.-L. Xu, H.-L. Li, Electrodeposited nickel hydroxide on nickel foam with ultrahigh capacitance, Chemical Communications (48) (2008) 6537-6539. https://doi.org/10.1039/B815647F.

[46] Y.-Y. Yang, Z.-A. Hu, Z.-Y. Zhang, F.-H. Zhang, Y.-J. Zhang, P.-J. Liang, H.-Y. Zhang, H.-Y. Wu, Reduced graphene oxide–nickel oxide composites with high electrochemical capacitive performance, Materials Chemistry and Physics 133(1) (2012) 363-368.

https://doi.org/https://doi.org/10.1016/j.matchemphys.2012.01.039.

[47] W.-J. Zhou, M.-W. Xu, D.-D. Zhao, C.-L. Xu, H.-L. Li, Electrodeposition and characterization of ordered mesoporous cobalt hydroxide films on different substrates for supercapacitors, Microporous and Mesoporous Materials 117(1) (2009) 55-60. https://doi.org/https://doi.org/10.1016/j.micromeso.2008.06.004.

[48] X.L. Li, J.F. Liu, Y.D. Li, Low-temperature conversion synthesis of M(OH)2 (M=Ni, Co, Fe) nanoflakes and nanorods, Materials Chemistry and Physics 80(1) (2003) 222-227. https://doi.org/https://doi.org/10.1016/S0254-0584(02)00488-1.

[49] J.T. Sampanthar, H.C. Zeng, Arresting Butterfly-Like Intermediate Nanocrystals of β-Co(OH)2 via Ethylenediamine-Mediated Synthesis, Journal of the American Chemical Society 124(23) (2002) 6668-6675. https://doi.org/10.1021/ja012595j.

[50] J. Yang, C. Yu, X. Fan, C. Zhao, J. Qiu, Ultrafast Self-Assembly of Graphene Oxide-Induced Monolithic NiCo–Carbonate Hydroxide Nanowire Architectures with a Superior Volumetric Capacitance for Supercapacitors, Advanced Functional Materials 25(14) (2015) 2109-2116. https://doi.org/https://doi.org/10.1002/adfm.201404019.

[51] W. Lu, X. Li, F. Wei, K. Cheng, W. Li, Y. Zhou, W. Zheng, L. Pan, G. Zhang, Fast sulfurization of nickel foam-supported nickel-cobalt carbonate hydroxide nanowire array at room temperature for hydrogen evolution electrocatalysis, Electrochimica Acta 318 (2019) 252-261. https://doi.org/https://doi.org/10.1016/j.electacta.2019.06.088.

[52] Y. Yuan, R. Chen, H. Zhang, Q. Liu, J. Liu, J. Yu, C. Wang, Z. Sun, J. Wang, Hierarchical NiSe@Co2(CO3)(OH)2 heterogeneous nanowire arrays on nickel foam as electrodewith high areal capacitance for hybrid supercapacitors, Electrochimica Acta 294 (2019) 325-336. https://doi.org/https://doi.org/10.1016/j.electacta.2018.10.058.

[53] K.V. Sankar, Y. Seo, S.C. Lee, S. Liu, A. Kundu, C. Ray, S.C. Jun, Cobalt carbonate hydroxides as advanced battery-type materials for supercapatteries: Influence of morphology

on performance, Electrochimica Acta 259 (2018) 1037-1044. https://doi.org/https://doi.org/10.1016/j.electacta.2017.11.009.

[54] S. Liu, K.S. Hui, K.N. Hui, V.V. Jadhav, Q.X. Xia, J.M. Yun, Y.R. Cho, R.S. Mane, K.H. Kim, Facile Synthesis of Microsphere Copper Cobalt Carbonate Hydroxides Electrode for Asymmetric Supercapacitor, Electrochimica Acta 188 (2016) 898-908. https://doi.org/https://doi.org/10.1016/j.electacta.2015.12.018.

[55] B. Ye, M. Huang, L. Fan, J. Lin, J. Wu, Co ions doped NiTe electrode material for asymmetric supercapacitor application, Journal of Alloys and Compounds 776 (2019) 993-1001. https://doi.org/https://doi.org/10.1016/j.jallcom.2018.10.358.

[56] S. Deshagani, P. Ghosal, M. Deepa, Altered crystal structure of nickel telluride by selenide doping and a poly(N-methylpyrrole) coating amplify supercapacitor performance, Electrochimica Acta 345 (2020) 136200. https://doi.org/https://doi.org/10.1016/j.electacta.2020.136200.

[57] B. Ye, C. Gong, M. Huang, Y. Tu, X. Zheng, L. Fan, J. Lin, J. Wu, Improved performance of a CoTe//AC asymmetric supercapacitor using a redox additive aqueous electrolyte, RSC advances 8(15) (2018) 7997-8006.

[58] C.C. Hu, C.Y. Cheng, Ideally pseudocapacitive behavior of amorphous hydrous cobalt-nickel oxide prepared by anodic deposition, Electrochem. Solid State Lett. 5(3) (2002) A43-A46. https://doi.org/10.1149/1.1448184.

[59] S. Ding, T. Zhu, J.S. Chen, Z. Wang, C. Yuan, X.W. Lou, Controlled synthesis of hierarchical NiO nanosheet hollow spheres with enhanced supercapacitive performance, Journal of Materials Chemistry 21(18) (2011) 6602-6606. https://doi.org/10.1039/C1JM00017A.

[60] G.X. Hu, C.H. Tang, C.X. Li, H.M. Li, Y. Wang, H. Gong, The Sol-Gel-Derived Nickel-Cobalt Oxides with High Supercapacitor Performances, J. Electrochem. Soc. 158(6) (2011) A695-A699. https://doi.org/10.1149/1.3574021.

[61] K. Chandra Majhi, P. Karfa, R. Madhuri, Bimetallic transition metal chalcogenide nanowire array: An effective catalyst for overall water splitting, Electrochimica Acta 318 (2019) 901-912. https://doi.org/https://doi.org/10.1016/j.electacta.2019.06.106.

[62] P. Bhol, M. Bhavya, S. Swain, M. Saxena, A.K. Samal, Modern chemical routes for the controlled synthesis of anisotropic bimetallic nanostructures and their application in catalysis, Frontiers in Chemistry 8 (2020) 357.

[63] T. Jin, Q. Han, L. Jiao, Binder-Free Electrodes for Advanced Sodium-Ion Batteries, Advanced Materials 32(3) (2020) 1806304. https://doi.org/https://doi.org/10.1002/adma.201806304.

[64] R.B. Rakhi, W. Chen, D. Cha, H.N. Alshareef, Substrate Dependent Self-Organization of Mesoporous Cobalt Oxide Nanowires with Remarkable Pseudocapacitance, Nano Letters 12(5) (2012) 2559-2567. https://doi.org/10.1021/nl300779a.

[65] J.-W. Lang, L.-B. Kong, W.-J. Wu, M. Liu, Y.-C. Luo, L. Kang, A facile approach to the preparation of loose-packed Ni(OH)2 nanoflake materials for electrochemical capacitors, Journal of Solid State Electrochemistry 13(2) (2008) 333. https://doi.org/10.1007/s10008-008-0560-0.

[66] I. Hussain, J.M. Lee, S. Iqbal, H.S. Kim, S.W. Jang, J.Y. Jung, H.J. An, C. Lamiel, S.G. Mohamed, Y.R. Lee, J.-J. Shim, Preserved crystal phase and morphology: Electrochemical influence of copper and iron co-doped cobalt oxide and its supercapacitor applications, Electrochimica Acta 340 (2020) 135953. https://doi.org/https://doi.org/10.1016/j.electacta.2020.135953.

[67] J. Cao, J. Li, L. Zhou, Y. Xi, X. Cao, Y. Zhang, W. Han, Tunable agglomeration of Co3O4 nanowires as the growing core for in-situ formation of Co2NiO4 assembled with polyaniline-derived carbonaceous fibers as the high-performance asymmetric supercapacitors, Journal of Alloys and Compounds 853 (2021) 157210. https://doi.org/https://doi.org/10.1016/j.jallcom.2020.157210.

[68] B. Ramulu, G. Nagaraju, S. Chandra Sekhar, S.K. Hussain, D. Narsimulu, J.S. Yu, Synergistic Effects of Cobalt Molybdate@Phosphate Core–Shell Architectures with Ultrahigh Capacity for Rechargeable Hybrid Supercapacitors, ACS Applied Materials & Interfaces 11(44) (2019) 41245-41257. https://doi.org/10.1021/acsami.9b11707.

[69] S.-B. Xia, S.-W. Yu, L.-F. Yao, F.-S. Li, X. Li, F.-X. Cheng, X. Shen, C.-K. Sun, H. Guo, J.-J. Liu, Robust hexagonal nut-shaped titanium(IV) MOF with porous structure for ultra-high performance lithium storage, Electrochimica Acta 296 (2019) 746-754. https://doi.org/https://doi.org/10.1016/j.electacta.2018.11.135.

[70] M.Z. Iqbal, S.S. Haider, S. Siddique, M.R.A. Karim, S. Zakar, M. Tayyab, M.M. Faisal, M. Sulman, A. Khan, M. Baghayeri, M.A. Kamran, T. Alherbi, M.J. Iqbal, T. Hussain, Capacitive and diffusion-controlled mechanism of strontium oxide based symmetric and asymmetric devices, Journal of Energy Storage 27 (2020) 101056. https://doi.org/https://doi.org/10.1016/j.est.2019.101056.

[71] G.K. Veerasubramani, A. Chandrasekhar, S. M. S. P, Y.S. Mok, S.J. Kim, Liquid electrolyte mediated flexible pouch-type hybrid supercapacitor based on binderless core–shell nanostructures assembled with honeycomb-like porous carbon, Journal of Materials Chemistry A 5(22) (2017) 11100-11113. https://doi.org/10.1039/C7TA01308F.

[72] H. Peng, G. Ma, K. Sun, Z. Zhang, J. Li, X. Zhou, Z. Lei, A novel aqueous asymmetric supercapacitor based on petal-like cobalt selenide nanosheets and nitrogen-doped porous

carbon networks electrodes, Journal of Power Sources 297 (2015) 351-358. https://doi.org/https://doi.org/10.1016/j.jpowsour.2015.08.025.

[73] Y. Zhu, Z. Wu, M. Jing, X. Yang, W. Song, X. Ji, Mesoporous NiCo2S4 nanoparticles as high-performance electrode materials for supercapacitors, Journal of Power Sources 273 (2015) 584-590. https://doi.org/https://doi.org/10.1016/j.jpowsour.2014.09.144.

[74] Z. Wu, X. Pu, X. Ji, Y. Zhu, M. Jing, Q. Chen, F. Jiao, High Energy Density Asymmetric Supercapacitors From Mesoporous NiCo2S4 Nanosheets, Electrochimica Acta 174 (2015) 238-245. https://doi.org/https://doi.org/10.1016/j.electacta.2015.06.011.

[75] K. Xu, W. Li, Q. Liu, B. Li, X. Liu, L. An, Z. Chen, R. Zou, J. Hu, Hierarchical mesoporous NiCo2O4@MnO2 core–shell nanowire arrays on nickel foam for aqueous asymmetric supercapacitors, Journal of Materials Chemistry A 2(13) (2014) 4795-4802. https://doi.org/10.1039/C3TA14647B.

[76] Y.-Y. Xie, Q.-S. Liu, D.-L. Li, G. Wu, S.-C. Chen, Y.-Z. Wang, Structural and electronic engineering towards high-efficiency metal-free electrocatalysts for boosting oxygen evolution, Chemical Engineering Journal 450 (2022) 138063. https://doi.org/https://doi.org/10.1016/j.cej.2022.138063.

[77] J.-Y. Zhang, L. Lv, Y. Tian, Z. Li, X. Ao, Y. Lan, J. Jiang, C. Wang, Rational Design of Cobalt–Iron Selenides for Highly Efficient Electrochemical Water Oxidation, ACS Applied Materials & Interfaces 9(39) (2017) 33833-33840. https://doi.org/10.1021/acsami.7b08917.

[78] S. Kapse, B. Benny, P. Mandal, R. Thapa, Design principle of MoS2/C heterostructure to enhance the quantum capacitance for supercapacitor application, Journal of Energy Storage 44 (2021) 103476. https://doi.org/https://doi.org/10.1016/j.est.2021.103476.

[79] R. Samal, M. Bhat, S. Kapse, R. Thapa, D.J. Late, C. Sekhar Rout, Enhanced energy storage performance and theoretical studies of 3D cuboidal manganese diselenides embedded

1226 with multiwalled carbon nanotubes, Journal of Colloid and Interface Science 598 (2021) 500-
1227 510. https://doi.org/https://doi.org/10.1016/j.jcis.2021.04.024.
1228 [80] S. Sarkar, A. Biswas, E.E. Siddharthan, R. Thapa, R.S. Dey, Strategic Modulation of
1229 Target-Specific Isolated Fe,Co Single-Atom Active Sites for Oxygen Electrocatalysis
1230 Impacting High Power Zn–Air Battery, ACS Nano 16(5) (2022) 7890-7903.
1231 https://doi.org/10.1021/acsnano.2c00547.
1232 [81] N. Ullah, W. Zhao, X. Lu, C.J. Oluigbo, S.A. Shah, M. Zhang, J. Xie, Y. Xu, In situ growth
1233 of M-MO (M = Ni, Co) in 3D graphene as a competent bifunctional electrocatalyst for OER
1234 and HER, Electrochimica Acta 298 (2019) 163-171.
1235 https://doi.org/https://doi.org/10.1016/j.electacta.2018.12.053.
1236 [82] S. Kapse, S. Janwari, U.V. Waghmare, R. Thapa, Energy parameter and electronic
1237 descriptor for carbon based catalyst predicted using QM/ML, Applied Catalysis B:
1238 Environmental 286 (2021) 119866.
1239 https://doi.org/https://doi.org/10.1016/j.apcatb.2020.119866.
1240 [83] B. Hammer, J.K. Norskov, Why gold is the noblest of all the metals, Nature 376(6537)
1241 (1995) 238-240.